A new reference model for the evolution of oceanic lithosphere in a cooling Earth

Tomoko Korenaga[1], Jun Korenaga[1], Hitoshi Kawakatsu[2], and Makoto Yamano[2]

[1]Department of Earth and Planetary Sciences, Yale University, New Haven, Connecticut, USA
[2]Earthquake Research Institute, University of Tokyo, Tokyo, Japan

Key Points:

- A new reference model for the evolution of normal oceanic lithosphere is proposed.
- The model is based solely on thermal conduction and yet free of unphysical boundary conditions.
- The model incorporates the effects of incomplete viscous relaxation, radiogenic heating, and secular cooling.

Corresponding author: Tomoko Korenaga, tomoko.korenaga@yale.edu

Abstract

We present a new reference model for the evolution of oceanic lithosphere, which incorporates the effects of incomplete viscous relaxation, radiogenic heating, and secular cooling. The new reference model is based solely on thermal conduction, i.e., without involving the occurrence of small-scale convection, and unlike the plate model, it does not contain unphysical boundary conditions. Yet, our model can explain both bathymetry and heat flow data on the normal seafloor. The success of the new model owes to the use of realistic material properties in conduction modeling as well as the consideration of all of major processes that take place ubiquitously beneath seafloor. The effect of secular cooling on the bathymetry of old seafloor is particularly notable. Whereas secular cooling brings only weak temperature variations with an amplitude of $\sim$20 K, it can nonetheless affect global bathymetry substantially owing to the deep sensitivity of long-wavelength topography kernels. We suggest that the well-known fact that Earth has been cooling, which was not considered in any of previous reference models, may be the key to the long-standing puzzle of seafloor flattening. The new reference model is expected to be useful to better quantify the impact of the emplacement of hotspot islands and oceanic plateaus, the effect of small-scale convection, and the regional history of secular cooling in the convecting mantle.

1 Introduction

The ocean basins constitute $\sim$60% of the Earth's surface, and because its capacity defines the volume of oceans, the evolution of ocean basins is one of the important factors controlling surface environment, e.g., the extent of dry landmasses (e.g., Parsons, 1982; Schubert & Reymer, 1985; Galer, 1991; Harrison, 1999; Flament et al., 2008; Korenaga et al., 2017). The primary feature of seafloor topography can be explained by the simple conductive cooling of the suboceanic mantle (e.g., Davis & Lister, 1974). However, the older part ($>\sim$70 Ma ago) of seafloor depth tends to be shallower than predicted by the simple half-space cooling model (Parsons & Sclater, 1977; Stein & Stein, 1992). The deviations from the model are known as "depth anomalies" or "seafloor flattening", and a variety of ideas have been proposed to explain the anomalous behavior of the old seafloor, including small-scale convection (Parsons & McKenzie, 1978; Davaille & Jaupart, 1994), reheating by mantle plumes (Heestand & Crough, 1981; Schroeder, 1984; Davies, 1988a; Smith & Sandwell, 1997), radiogenic heat production (Crough, 1977; Forsyth, 1977; Jarvis & Peltier, 1982), and the combination of radiogenic heating and small-scale convection (Huang & Zhong, 2005; Korenaga, 2015). The deviation has often been modeled by the so-called plate model (Langseth et al., 1966; McKenzie, 1967), in which temperature is fixed at a depth of $\sim$100 km. The plate model is described by a simple analytical formula, and it is widely adapted as a ref-

erence model to represent averaged global depth and heat flow. The model is also used in a wide range of geophysical and geochemical studies (e.g., McKenzie, 1978; Watts et al., 1980; McNutt, 1984; Davies & von Blanckenburg, 1995; Kawakatsu et al., 2009; Syracuse et al., 2010; Yamamoto et al., 2014; Sarafian et al., 2015; Mehouachi & Singh, 2018). Despite its long-standing popularity, the plate model is a phenomenological model designed to fit the present-day seafloor, and as such, it is unclear whether the model can be applied to model the behavior of ocean basins in the distant past (e.g., Korenaga et al., 2017).

In this paper, we present a new reference model for the evolution of oceanic lithosphere, which is based on the physics of thermal conduction with no artificial boundary condition and yet can explain available surface observations for 'normal' seafloor of all ages. This new reference model is built on two different developments. First, Korenaga and Korenaga (2008) introduced a new method of defining 'normal' seafloor using statistical correlation. Their reexamination of age-depth relationship yielded a subsidence rate of $\sim$320 m Ma$^{-1/2}$ for seafloor younger than $\sim$70 Ma ago, which is $\sim$10% lower than conventional estimates (Parsons & Sclater, 1977; Stein & Stein, 1992; Carlson & Johnson, 1994; Smith & Sandwell, 1997). Second, Korenaga and Korenaga (2016) suggested that the subsidence rate should actually be as high as $\sim$400-500 m Ma$^{-1/2}$, based on theoretical calculation of half-space cooling with variable material properties and the spinel-to-garnet phase transition. They also found that this difference between observed and theoretical subsidence rates could be explained by taking into account the effects of incomplete viscous relaxation, radiogenic heat production, and secular cooling, all of which are expected for the normal mantle. Incomplete viscous relaxation results from the strong temperature dependence of mantle rheology (e.g., Pollack, 1980; Korenaga, 2007a), radiogenic heat production is constrained by the the compositional model of Earth's mantle (e.g., Jochum et al., 1983; McDonough & Sun, 1995; Lyubetskaya & Korenaga, 2007b), and secular cooling is required by the present-day thermal budget of Earth (e.g., Korenaga, 2008; Jaupart et al., 2015). The analysis of Korenaga and Korenaga (2016) was, however, limited to young seafloor, and in this study, by extending their approach further to older seafloor, we show that it is possible to explain both seafloor depth and surface heat flow data on normal seafloor of all ages.

The structure of this paper is as follows. First, we begin with our theoretical formulation. We explain how to parameterize the numerical solution of half-space cooling with variable material properties and how to correct for the effects of radiogenic heating and secular cooling. We also describe how to compute corresponding seafloor topography using instantaneous Stokes flow. Second, we describe the processing of global marine geophysical data, from which we extract the age-depth and age-heat flow relations for normal seafloor. Then, we show that such relations can be explained by our model of conductive

cooling, with reasonable amounts of radiogenic heat production and secular cooling. Being able to satisfy both seafloor and heat flow data also allows us to construct a reference model for thermal structure. Finally, we discuss the significance of this new reference model in relation to previous models and the possibility of testing it by seismological means.

2 Theory

Similar to traditional reference models such as the half-space cooling model and the plate model, our reference model is based only on the physics of thermal conduction, without the occurrence of sublithospheric convection. Given the current understanding of upper mantle rheology (Karato & Wu, 1993; Hirth & Kohlstedt, 2003; Jain et al., 2019), the onset of small-scale, sublithospheric convection is possible within a typical lifetime of oceanic plate (e.g., Korenaga & Jordan, 2003; Huang et al., 2003), and thus it may be tempting to include the effect of sublithospheric convection when building a reference model for the evolution of normal oceanic lithosphere (e.g., Korenaga, 2020). However, the uncertainty of upper mantle rheology is still substantial (Jain et al., 2019), and incorporating such a dynamic effect in a reference model is probably premature. The exclusion of sublithospheric convection from consideration may also be preferable from a practical point of view, because a reference model based purely on thermal conduction is easily reproducible.

Our theoretical formulation follows closely that of Korenaga and Korenaga (2016), which extends the classic half-space cooling model with the following seven additional features: (1) the presence of 7-km-thick oceanic crust, (2) compositional variations associated with melt extraction, (3) spatially variable thermodynamic properties, (4) the possibility of spinel-to-garnet phase transition, (5) the effect of incomplete viscous relaxation on effective thermal expansivity, (6) radiogenic heating, and (7) secular cooling. The first two are related to the generation of oceanic crust by the partial melting of the mantle upwelling beneath mid-ocean ridges. The thermal diffusivity of oceanic crust is lower than that of the mantle, so the presence of oceanic crust significantly affects the thermal structure of oceanic lithosphere and thus surface heat flow (Grose & Afonso, 2013). Compositional variations within the mantle have only limited effects on thermal structure; they are more relevant to seafloor subsidence because an accurate knowledge of mantle composition is important when considering the spinel-to-garnet phase transition, which affects the rate of subsidence. Spatially variable thermodynamic properties include temperature-dependent specific heat, temperature- and pressure-dependent thermal conductivity with radiative contribution, and temperature-, pressure-, and composition-dependent density, all of which are important for heat flow and subsidence. The effect of incomplete viscous relaxation is largely limited to seafloor subsidence. The last two items, radiogenic heating and secular cooling, both affect thermal struc-

ture, but they have negligible influence on surface heat flow. Because of their distributed influence on thermal structure, however, they can affect seafloor subsidence considerably.

Among the above seven features, Korenaga and Korenaga (2016) incorporated the first four into their modeling of thermal conduction, and they incorporated the remaining three when calculating seafloor subsidence. We also adopt this approach here because it allows us to efficiently evaluate the influence of these three. Our modeling of thermal conduction is the same as that done by Korenaga and Korenaga (2016), with the only difference being the duration of modeling and its depth extent. The main focus of Korenaga and Korenaga (2016) was the evolution of young ocean lithosphere, so their modeling results cover only up to 100 Ma; we model up to 200 Ma in this study. As the technical details of conduction modeling can be found in Korenaga and Korenaga (2016), we do not repeat them here. Instead, we provide a parameterization of our modeling results so that others do not need to perform the underlying heat transport modeling. In what follows, we describe our parameterization in three steps, first how we parameterize the thermal structure and heat flow of the half-space cooling model with variable material properties, then how such parameterization may be corrected for the effects of internal heating and secular cooling, and finally how our prediction for seafloor subsidence can be parameterized.

2.1 Half-Space Cooling with Variable Material Properties

As in Korenaga and Korenaga (2016), the thermal evolution of the suboceanic mantle is modeled by solving the following one-dimensional equation of thermal conduction:

$$\rho(P,T)C_P(P,T)\frac{\partial T}{\partial t} = \frac{\partial}{\partial z}\left(k(P,T)\frac{\partial T}{\partial z}\right), \tag{1}$$

where ρ, C_P, k, P, T, t, and z are density, specific heat, thermal conductivity, pressure, temperature, time, and depth, respectively. See Korenaga and Korenaga (2016) for how density, specific heat, and thermal conductivity vary with pressure and temperature. Note that internal heating is not considered at this stage. The model spans from the seafloor (z = 0) to the depth of 400 km, and the initial temperature profile is the adiabat with the potential temperature of 1623 K (1350 °C) (Herzberg et al., 2007), and the surface temperature is fixed at 273 K (0 °C). Using a finite difference approximation with a vertical spacing of 1 km and a time step of 5000 years, we integrate the equation from t = 0 to 200 Ma (Figure 1).

We were able to obtain a reasonably approximate parameterization to our numerical solution, by modifying the conventional half-space solution with a depth-dependent

thermal diffusivity as

$$T^0_{\mathrm{KK16}}(t,z) = T_s + \Delta T \mathrm{erf}\left(\frac{z}{2\sqrt{\kappa(z)t}}\right) + a_1 z + a_2 z^2, \tag{2}$$

where T_s is the surface temperature (273 K), ΔT is 1350 K, erf$(\cdot)$ is the error function, a_1 = 0.602 $\times$ 10^{-3} K m^{-1}, a_2 = -6.045 $\times$ 10^{-10} K m^{-2}, and for $z < 7$ km, $\kappa(z)$ = 3.45 $\times$ 10^{-7} m^2 s^{-1}, and for $z \geq 7$ km,

$$\kappa(z) = \kappa_0 \sum_{n=0}^{6} b_n (z/z_{\mathrm{ref}})^{\frac{n}{2}} \tag{3}$$

with κ_0 = 2.23 $\times$ 10^{-6} m^2 s^{-1}, z_{ref} = 10^5 m, b_0 = -1.255, b_1 = 9.944, b_2 = -25.0619, b_3 = 32.2944, b_4 = -22.2017, b_5 = 7.7336, and b_6 = -1.0622. The terms $a_1 z + a_2 z^2$ represent the adiabatic component. The subscript 'KK16' denotes that this parameterization is based on the numerical solution of Korenaga and Korenaga (2016), and the superscript '0' signifies that this equation serves as a baseline, to be corrected later for additional effects. As it may be understood from the units of these constants, here temperature T is in K, time t is in seconds, and depth z is in meters. The thermal structure according to this approximation is also shown in Figure 1a. The root-mean-square (RMS) error of the approximation is $\sim$0.6 %, and the difference from the original numerical solution is below $\sim$10 K for older ($t > 80$ Ma) part.

Similarly, we found that surface heat flow could be approximated, with a RMS error of $\sim$1.4 %, as

$$q^0_{\mathrm{KK16}}(t) = \frac{C(t)}{\sqrt{t}} \tag{4}$$

where q is in mW m^{-2}, t is time in Ma, and

$$C(t) = \sum_{n=0}^{4} c_n (\sqrt{t})^n, \tag{5}$$

with c_0 = 338.4, c_1 = 66.7, c_2 = -8.26, c_3 = 0.53, and c_4 = -0.013. Note that this approximation is valid only for $t \leq 200$ Ma.

2.2 Effects of Radiogenic Heating and Secular Cooling

Both radiogenic heating and secular cooling modify the above thermal structure and surface heat flow only slightly. To see this quantitatively, consider the following classic half-space cooling solution,

$$T_1(t,z) = T_s + \Delta T \mathrm{erf}\left(\frac{z}{2\sqrt{\kappa t}}\right). \tag{6}$$

With these two additional effects, the above solution may be modified to (e.g., Carslaw & Jaeger, 1959):

$$\begin{aligned} T_2(t,z) &= T_s + \Delta T \mathrm{erf}\left(\frac{z}{2\sqrt{\kappa t}}\right) \\ &\quad + \frac{H}{C_P}\left[\left(t+\frac{z^2}{2\kappa}\right)\mathrm{erf}\left(\frac{z}{2\sqrt{\kappa t}}\right) + z\sqrt{\frac{t}{\pi\kappa}}\exp\left(-\frac{z^2}{4\kappa t}\right) - \frac{z^2}{2\kappa}\right] \\ &\quad + \delta T(t)\mathrm{erf}\left(\frac{z}{2\sqrt{\kappa t}}\right), \end{aligned} \tag{7}$$

where the third and fourth terms on the right-hand side represent, respectively, the effects of radiogenic heating, H, and secular cooling, $\delta T(t)$. For the sake of simplicity, the effect of adiabatic compression is not considered here; this is consistent with the incompressible fluid approximation used later for topography calculation. When constructing a reference model for the thermal structure of oceanic lithosphere, time t is also used as the seafloor age, and this convention is followed here as well. The effect of secular cooling is then modeled by having $\delta T(t) > 0$ for $t > 0$; i.e., it appears as secular heating as we go deeper in time. Also, strictly speaking, the amount of radiogenic heating H should be modified as a function of seafloor age, but as noted by Korenaga and Korenaga (2016), such change is of negligible influence for the lifetime of seafloor.

The concentration of heating-producing elements in the present-day convecting mantle is estimated to be 9.7 ppb U, 30 ppb Th, and 102 ppm K (Korenaga, 2017b), which amounts to the heat production of 2.09×10^{-12} W kg^{-1}. This is lower than the heat production of the primitive mantle (e.g., 4.92×10^{-12} W kg^{-1} corresponding to the model of McDonough and Sun (1995)), because of the extraction of enriched continental crust, but is higher than that of the depleted source mantle for mid-ocean ridge basalts (MORB) (e.g., 0.69×10^{-12} W kg^{-1} corresponding to the model of Workman and Hart (2005)), because the depleted MORB-source mantle refers to the most depleted component within the convecting mantle. The above estimate of Korenaga (2017b) for the convecting mantle has the uncertainty of $\sim$40 %; because it is based on a mass balance calculation involving the composition models of the primitive mantle (Lyubetskaya & Korenaga, 2007a) and the continental crust (Rudnick & Gao, 2003), it inherits the uncertainties of both models. The internal heating term in equation (7) looks complicated, but its growth is bounded by Ht/C_P. With the heat production of 2×10^{-12} W kg^{-1} and the specific heat of 1200 J K^{-1} kg^{-1}, therefore, the mantle temperature goes up by only $\sim$5 K every 100 Ma.

Heat loss from Earth's surface to space has been greater than radiogenic heat production within Earth, at least for the last three billion years or so (Herzberg et al., 2010), leading to the long-term cooling of Earth as a whole. The term 'secular cooling' refers to

this long-term, global cooling. According to the petrological estimate of Herzberg et al. (2010), the mantle has been cooling at the rate of 100-150 K Ga^{-1} for the last one billion years (note: the average cooling rate over the last three billion years is ∼50-100 K Ga^{-1}), and this recent cooling rate is consistent with the present-day thermal budget of Earth (Korenaga, 2008; Jaupart et al., 2015). That is, the convecting mantle was ∼10-15 K hotter, on average, 100 Ma ago, and this secular cooling effect can easily be incorporated into the half-space cooling model by varying $\delta T(t)$ in equation (7). For the secular cooling rate of 100 K Ga^{-1}, for example, $\delta T(t)$ varies linearly from 0 at t = 0 to 20 K at t = 200 Ma. The magnitude of cooling during the life time of oceanic lithosphere is small, but secular cooling appears to have left a discernible trace in the thickness of oceanic crust (Van Avendonk et al., 2017).

Surface heat flow corresponding to the classic half-space solution of equation (6) is given by

$$q_1(t) = \frac{k\Delta T}{\sqrt{\pi\kappa t}}, \tag{8}$$

where k is thermal conductivity, and that corresponding to the equation (7) is by

$$q_2(t) = \frac{k\Delta T}{\sqrt{\pi\kappa t}} + \frac{2kH}{C_P}\sqrt{\frac{t}{\pi\kappa}} + \frac{k\delta T(t)}{\sqrt{\pi\kappa t}}. \tag{9}$$

The combined effects of internal heating and secular cooling are mostly to raise the temperature of the sublithospheric mantle beneath older seafloor, by ∼20 K every 100 Ma, which is dwarfed by the temperature variation across the lithosphere (Figure 1). Their effects on surface heat flow are limited as well, with only ∼2 % increase every 100 Ma. We may thus incorporate these effects into our numerical solutions by multiplying $T_2(t)/T_1(t)$ to thermal structure and $q_2(t)/q_1(t)$ to surface heat flow.

2.3 Notes on Radiogenic Heating and Secular Cooling

As in the modeling studies of Korenaga (2015) and Korenaga and Korenaga (2016), we use the thermal structure predicted by equation (7) for the whole mantle. This is equivalent to assuming that the sublithospheric mantle, down to the core-mantle boundary, moves laterally with the overlying plate, which appears to be unrealistic. This idealized model setting is, however, motivated by likely complications associated with mantle convection and can be considered appropriate when building a reference model, as explained below. We note that this assumption of the whole-mantle domain is guided primarily by its simplicity, and given the depth sensitivity of topography kernels (§2.4), it can be relaxed considerably (§4; cf. Figure 7b).

When mantle convection is simulated within a closed model domain, subducted materials return through the deep mantle to a mid-ocean ridge, and the mantle beneath old oceanic lithosphere is enclosed by and left from this global circulation, thereby being cooled less efficiently and accumulating more heat compared to the other parts of the mantle (e.g., Lowman et al., 2003; Huang & Zhong, 2005). That is, positive thermal anomalies result from the mantle beneath old oceanic lithosphere being even older, and such 'trapped heat' could exist in the actual mantle if a return flow from a subduction zone to a ridge is maintained for a sufficiently long time (e.g., Morishige et al., 2010). This trapped heat is a common feature in mantle convection models with internal heating, and one representative example is shown in Figure 2a. This model is set up similarly to those studied by (Huang & Zhong, 2005), but unlike their steady-state models, it exhibits secular cooling at a rate of $\sim$50 K Ga^{-1} (for the further details of numerical simulation, see Supporting Information; Figure S1). Because both of internal heat production and secular cooling tend to be 'trapped' in this type of mantle circulation, the sublithospheric mantle beneath the older part of seafloor is hotter than that beneath the ridge axis by $\sim$25-55 K (Figure 2c), which leads to $\sim$1 km shallowing of seafloor with respect to the case of no internal heating and secular cooling (Figure 2g). For comparison, temperature variations for our reference model (i.e., whole-mantle lateral flow with the same amount of internal heating and secular cooling for this convection model) is shown in Figure 2e, and the corresponding subsidence behavior in Figure 2g. The amplitude of sublithospheric temperature variations in the reference model is only $\sim$20 K, but because it is uniformly distributed throughout the mantle, its effect of subsidence is comparable to that of greater but spatially heterogeneous temperature variations seen in Figure 2a. In this particular simulation example, the effect of trapped heat extends below young seafloor, reducing the subsidence rate as a whole (Figure 2g).

For the case Figure 2a, a realistic temperature dependence of mantle viscosity (the Frank-Kamenetskii parameter of 18, which is equivalent to the activation energy of $\sim$300 kJ mol^{-1}; the definition of the Frank-Kamenetskii parameter is given in Supporting Information) is used, and for comparison, another case with a much reduced temperature dependence (the Frank-Kamenetskii parameter of 6) is shown in Figure 2b. The reduced temperature dependence facilitates small-scale convection, and resulting cold downwellings efficiently mix the sublithospheric mantle, erasing the effect of internal heating and secular cooling (Figure 2d). Seafloor shallowing is still observed at older seafloor (Figure 2h), and this is owing to the extensive thinning of lithosphere by delamination. For their steady-state convection models, (Huang & Zhong, 2005) also used the Frank-Kamenetskii parameter of $\sim$6, but we note that this temperature dependence corresponds to the activation energy of $\sim$100 kJ mol^{-1}, which is at odds with experimental rock mechanics (e.g., Karato & Wu, 1993; Hirth & Kohlstedt, 2003; Jain et al., 2019). Thus, the intensity of

lithospheric delamination and resulting convective mixing seen in Figure 2b should be regarded as an extreme end-member (see Figures S2 and S3 for further examples of convection snapshots). Note that the intensity of lithospheric delamination is controlled solely by the activation energy and is independent of asthenospheric viscosity (e.g., Solomatov & Moresi, 2000) (see also Figure 5c of Korenaga and Jordan (2004)).

The difference between two convection snapshots shown in Figures 2a and 2b represents only a small fraction of variations expected for modeling with a closed domain, because this type of modeling involves a fair number of parameters such as the amount of internal heating, plate speed, mantle rheology, the temperature of the core-mantle boundary, and the aspect ratio of the model. Even by exploring the effects of these parameters, however, modeling with a 2-D closed domain is inherently limited because the actual mantle convection takes place in a 3-D spherical shell with evolving plate boundaries. For example, the pattern of mantle circulation leading to trapped heat discussed above does not apply to the Atlantic-type seafloor, and the suboceanic mantle near passive margins may instead have been affected by supercontinental insulation (e.g., Coltice et al., 2007; Korenaga, 2007b; Van Avendonk et al., 2017).

In light of this complexity of time-dependent mantle convection, it is difficult to decide on an ideal model setup for the evolution of the suboceanic mantle. Traditional reference models such as the half-space cooling and plate models have focused on the lithospheric part, but as discussed at length in §2.4, long-wavelength surface topography is sensitive to deep-mantle density anomalies, so it is desirable to include the sublithospheric part in a reference model. Radiogenic heating and secular cooling are both important factors in the thermal budget of Earth, so a reference model should honor them. Considering them in the framework of a closed model domain (e.g., Figure 2a), however, would lead to an overly complicated model with return flow and core heat flux. A closed model domain also has a tendency to overemphasize the effect of internal heating and secular cooling under old seafloor. Small-scale convection could alleviate this trapped heat effect, but its efficacy is currently uncertain (§5.3). Instead of trapped heat, the mantle beneath passive margins could be influenced by supercontinental insulation, which is a large-scale manifestation of radiogenic heating and secular cooling. Given these realistic complications expected for mantle convection, our assumption of whole-mantle lateral advection can provide a simple reference state that includes the effect of radiogenic heating and secular cooling and allows us to demonstrate the importance of deep-mantle thermal anomalies on surface topography. Being simple also facilitates to measure the effect of neglected processes, such as trapped heat, supercontinental insulation, small-scale convection, mantle plumes, and deep return flow. Traditional half-space cooling and plate models are both simple, but the former cannot explain

the depths of old seafloor, thereby being an incomplete reference model for oceanic lithosphere, and the latter is physically problematic (§5.2).

Our reference model for the evolution of the suboceanic mantle starts with a mantle column with a constant potential temperature under a mid-ocean ridge. In absence of radiogenic heating and secular heating, the sublithospheric mantle retains this initial potential temperature. If radioactive isotopes are uniformly distributed through the mantle, the entire mantle is heated uniformly. Because the thermal evolution of the suboceanic mantle is measured with respect to the mantle column beneath the present-day ridge, however, the mantle beneath 100 Ma-old seafloor would have been subject to 100 Ma-worth radiogenic heating, if its initial potential temperature beneath a ridge was the same as the present-day potential temperature beneath a ridge. On top of this, the initial potential temperature beneath a ridge would vary with time in the presence of secular cooling. The use of the mantle column beneath a mid-ocean ridge as a reference is appropriate from a petrological aspect; estimates on the present-day mantle potential temperature are based on the petrology of present-day MORB (e.g., Herzberg et al., 2007).

The secular cooling of the mantle occurs because the surface heat loss is greater than the combination of radiogenic heating and core heat flux. It may be worth noting that the secular cooling of the suboceanic mantle does not result directly from conductive cooling through oceanic lithosphere. Oceanic lithosphere grows by conductive cooling, but the mantle well below the growing lithosphere is not affected by this conductive cooling [e.g., equation (6)]. Secular cooling manifests when subducted, initially cold materials do not recover their original potential temperature beneath a mid-ocean ridge even after mixing with the ambient mantle and receiving radiogenic heating and core heat flux. This mantle mixing process is outside the scope of our reference model because, as indicated in the above, it would involve the complexity of mantle convection. In our model, the effect of secular cooling appears simply as the time-varying initial potential temperature beneath a mid-ocean ridge.

Mantle circulation implied by our reference model, if taken literately, would not make much sense, because the effect of secular cooling 'magically' shows up in the mantle beneath a ridge axis, and because the whole mantle moves laterally at the same speed with the surface plate motion. It should be regarded as one possible abstraction that extracts the essence of radiogenic heating and secular cooling on the evolution of the suboceanic mantle. Such an abstraction is probably important, given the regional variations of seafloor subsidence. Marty and Cazenave (1989) divided the seafloor into a total of 32 tectonic corridors (with common ancestral mid-ocean ridge segments) and found that their regional subsidence rates varied widely from $\sim$150 m Ma$^{-1/2}$ to $\sim$430 m Ma$^{-1/2}$. The

global subsidence rate of $\sim$320 m Ma$^{-1/2}$ is a result of averaging out these regional variations, and a model that can explain such a subsidence rate is rather a hypothetical entity, because regions subsiding with the global rate of $\sim$320 m Ma$^{-1/2}$ are actually rare. Our reference model prescribes the effect of radiogenic heating and secular cooling uniformly to the entire depth of the sublithospheric mantle as a function of seafloor age. One may argue that this is excessive because only the shallow mantle would move together with a surface plate, but an opposite argument is also possible if one takes into account the influence of trapped heat and supercontinental insulation, both of which could potentially be significant for the thermal state of the present-day mantle. Thus, our reference model may be considered as a neutral choice.

As mentioned in §2.2, the cooling history of the upper mantle based on the petrology of Precambrian lavas indicates the secular cooling of 100-150 K Ga^{-1} for the last one billion years (Herzberg et al., 2010), and this level of secular cooling is actually required by the imbalance of heat sources and sinks in the present-day mantle; the amount of radioactive isotopes within Earth is simply too low to achieve a thermal equilibrium (e.g., McDonough & Sun, 1995; Lyubetskaya & Korenaga, 2007b). Recently, Aulbach and Arndt (2019) suggested a much reduced rate of secular cooling ($\sim$40 K Ga^{-1}) based on the petrology of eclogite xenoliths, but their interpretation assumes no fractional crystallization during the formation of oceanic crust, which is difficult to justify (Herzberg, 2019). Such a reduced cooling rate also implies that we need to violate geochemical and cosmochemical constraints on the chemical composition of Earth's mantle. We note that the rate of secular cooling does not have to be constant because both surface heat flow and radiogenic heating can vary with time, and the estimate of Herzberg et al. (2010) does suggest that secular cooling was negligible at $\sim$2.5-3 Ga. Thus, radiogenic heating likely played a far more important role in the evolution of the suboceanic mantle during the Archean (Rosas & Korenaga, 2021).

It is also important to properly recognize uncertainties associated with radiogenic heating in the mantle. The heat production of the depleted MORB-source mantle is estimated to be 1.03×10^{-12} W kg^{-1} and 0.69×10^{-12} W kg^{-1}, respectively, according to the chemical composition models of Salters and Stracke (2004) and Workman and Hart (2005), and given this, one may be tempted to think that the upper mantle would be characterized by this level of heat production. A few caveats are warranted on this issue. First, the model of Salters and Stracke (2004) is biased toward the depleted end-member of MORB samples (Korenaga, 2008), and that of Workman and Hart (2005) is based mainly on abyssal peridotites, thereby automatically excluding the contribution of more mafic lithologies, which are considered to be enriched in trace elements including heat-

producing isotopes (e.g., Helffrich & Wood, 2001; Sobolev et al., 2007). Second, both models involve a fair number of assumptions, such as the mode of mantle melting, the primitive mantle composition, and continental growth, yet these various sources of uncertainty are not propagated into the uncertainty of the published models. The primitive mantle composition itself has one standard deviation of $\sim$17 % (Lyubetskaya & Korenaga, 2007a), and the models of continental growth have drastically been revised in recent years (e.g., Korenaga, 2018; Guo & Korenaga, 2020). Finally, the upper mantle is not necessarily occupied predominantly by the depleted MORB-source mantle; the enriched domain of the mantle may be spatially dispersed (e.g., Helffrich & Wood, 2001; Ito & Mahoney, 2005). Because of these issues, our adopted heat production for the present-day convecting mantle, which is derived simply as a difference between the heat production of the primitive mantle and that of the continental crust, may be regarded as a robust whole-mantle average.

2.4 Calculation of Surface Topography

We first note that seafloor depth corresponding to the thermal structure described by equation (2) may be approximated as

$$d^0_{\mathrm{KK16}}(t) = d_0 + d_1\sqrt{t} + d_2 \tanh(e_2 t), \tag{10}$$

where t is seafloor age in Ma, d_0 = 2600 m, d_1 = 409 m Ma$^{-1/2}$, d_2 = 930 m, and e_2 = 0.018 Ma^{-1}. This is based on thermal isostasy with a compressible medium (see Appendix B of Korenaga and Korenaga (2016)), and the zero-age depth d_0 is from the global data analysis of Korenaga and Korenaga (2008). The second and third terms on the right-hand side correspond to density changes from thermal contraction and the spinel-to-garnet phase transition, respectively. This approximation is valid up to t = 200 Ma, and its RMS error is $\sim$0.7 %. As noted by Korenaga and Korenaga (2016), half-space cooling with realistic material properties predicts too fast subsidence, with the subsidence rate of $\sim$400-500 m Ma$^{-1/2}$, whereas the observed subsidence rate is only $\sim$320 m Ma$^{-1/2}$ (Korenaga & Korenaga, 2008). They suggest that the discrepancy may be resolved if we consider the effects of incomplete viscous relaxation, internal heating, and secular cooling. The analysis of Korenaga and Korenaga (2016) is limited to seafloor younger than $\sim$70 Ma old, for which half-space cooling is traditionally thought to be adequate, and in this study, we extend their approach to seafloor of all ages.

It is straightforward to incorporate the effect of incomplete viscous relaxation. Because incomplete relaxation reduces the effective thermal expansivity of oceanic lithosphere (Korenaga, 2007a), its effect on subsidence is limited to the thermal

contraction part:

$$d^1_{\mathrm{KK16}}(t) = d_0 + d_1 f_{\mathrm{TC}} \sqrt{t} + d_2 \tanh(e_2 t), \tag{11}$$

where f_{TC} represents the degree of thermal contraction and can vary from 0 (no contraction) to 1 (complete contraction). A theoretical estimate based on viscoelastic modeling suggests that that incomplete viscous relaxation reduces effective thermal expansivity by $\sim$15-25 % (corresponding to f_{TC} of 0.75-0.85) for temperature-dependent viscosity with an activation energy of 300 kJ mol^{-1} (Korenaga, 2007a). This effect of incomplete viscous relaxation can be alleviated by brittle relaxation such as thermal cracking and normal faulting (Korenaga, 2007c, 2017a), but even in the limit of complete brittle relaxation, effective thermal expansivity is still reduced by $\sim$10-15 % (f_{TC} of 0.85-0.90) (Korenaga, 2007a). Given the current understanding of mantle rheology (Karato, 2008; Jain et al., 2019), the possibility of incomplete viscous relaxation is difficult to dismiss, but the extent of brittle relaxation remains to be resolved. As noted by Korenaga (2007c), thermal cracking alone would leave the stress state of oceanic lithosphere extensional, which would be inconsistent with the focal mechanisms of intraplate earthquakes, thereby calling for additional relaxation processes such as secondary thermal cracking enabled by serpentinization. Recently, Huang et al. (2015) reported the occurrence of shallow thrust and deep normal earthquakes within a $\sim$25 Ma-old oceanic lithosphere, which implies that brittle relaxation may be complete only at shallow depths. This would make sense because what hinders brittle relaxation is the confining pressure (i.e., difference between lithostatic and hydrostatic pressures), the influence of which is limited at shallow depths (i.e., up to a few km). We note that Mishra and Gordon (2016) argue that the observed azimuths of transform faults, which are consistent with their 'shrinking plate' hypothesis, invalidate the thermal cracking hypothesis of Korenaga (2007c), but their argument does not correctly represent the physics of thermal cracking. As explained above, complete brittle relaxation, which correspongs to a 'shrinking plate,' is likely at shallow depths, and thermal cracking takes part in such relaxation. Transform faults and fracture zones themselves are the most prominent examples of thermal cracking (Turcotte & Oxburgh, 1973; Turcotte, 1974), and the existence of other thermal cracks within oceanic lithosphere has been suggested by the spatial pattern of intermediate-depth earthquakes beneath northeastern Japan (Korenaga, 2017a) as well as an electromagnetic sounding of a Pacific lithosphere (Chesley et al., 2019). To summarize, effective thermal expansivity is definitely reduced by incomplete viscous relaxation, but it remains uncertain how this reduction would be moderated by subsequent brittle relaxation. Given this uncertainty, we vary f_{TC} in a range of 0.8-0.9.

Taking into account the effects of radiogenic heating and secular cooling is more involved. As seen in the previous section, their effects on thermal structure and surface heat

flow are small compared to temperature variations across the lithosphere. However, they can have a considerable influence on seafloor subsidence. This is because surface topography reflects vertically-integrated buoyancy; even a temperature difference of as small as 10 K could give rise to a notable difference in topography (and thus subsidence) because the temperature difference is distributed throughout the mantle column. When calculating seafloor subsidence caused by the growth of lithosphere, the concept of thermal isostasy is valid (e.g., Parsons & Daly, 1983), i.e., we can assume that all of buoyancy in the lithosphere contributes to surface topography, but to take into account the effect of additional buoyancy distributed throughout the mantle, it becomes necessary to calculate surface topography by solving instantaneous Stokes flow (e.g., Davies, 1988b). Here we incorporate the effects of radiogenic heating and secular cooling by comparing two such topography profiles, one corresponding to the thermal structure given by equation (6) and the other to the thermal structure by equation (7). Because the difference between these two structures resides mostly in the sublithospheric domain, its influence on surface topography may simply be added to equation (11) as

$$d^2_{\mathrm{KK16}}(t) = d_0 + d_1 f_{TC}\sqrt{t} + d_2 \tanh(e_2 t) + b_h(w_2^* - w_1^*), \tag{12}$$

where b_h is the topography scale, whereas w_1^* and w_2^* are nondimensional topography corresponding to the thermal structure of equations (6) and (7), respectively. The topography scale is defined as

$$b_h = \alpha \Delta T D \frac{\rho_m}{\rho_m - \rho_w}, \tag{13}$$

where α is thermal expansivity, D is the mantle depth, ρ_m is mantle density, and ρ_w is water density. The use of topography scale and nondimensional topography above stems from the fact that instantaneous Stokes flow is usually obtained by solving the nondimensional governing equations for mass and momentum conservation. As in Korenaga (2015) and Korenaga and Korenaga (2016), we use the two-dimensional finite element implementation of Stoke flow solver for incompressible fuild (Korenaga & Jordan, 2003); as noted earlier, the use of incompressible approximation is consistent with the omission of adiabatic compression in equations (6) and (7). To reduce the influence of side boundaries, we compute surface topography for seafloor with ages from zero to 300 Ma ago and retain results only up to 200 Ma ago. The aspect ratio of the model domain is either 4:1 or 8:1, i.e., the model width is four or eight times as large as the model depth, and the model is discretized with 400 $\times$ 100 or 800 $\times$ 100 uniform quadrilateral elements. In terms of a plate spanning from a mid-ocean ridge to 150 Ma old seafloor, the aspect ratio of 4:1 corresponds to the plate length of 5800 km, and that of 8:1 corresponds to the plate length of 11600 km. The top and bottom boundaries are free-slip, and the side boundaries are reflecting.

We refer to Korenaga (2015) for the further details of Stokes flow calculation, but there are three issues that deserve in-depth discussion here. First, surface topography is sensitive to an assumed viscosity structure, and given that the uncertainty of mantle viscosity is still quite large (e.g., Forte et al., 2015), we need to test a range of viscosity structure. Surface topography is only sensitive to the relative variations of viscosity; it is not sensitive to the absolute value of viscosity. We measure such relative variations with respect to the viscosity of asthenosphere. It is important to take into account the effect of strong lithosphere by using temperature-dependent viscosity, and in this study, we use the Frank-Kamenetskii parameter of 18, which corresponds to the activation energy of $\sim$300 kJ mol^{-1} (e.g., Karato & Wu, 1993). In addition, to explore the effect of depth-dependent viscosity, we increase the viscosity of the lower mantle by up to two orders of magnitude relative to that of the upper mantle. Second, because the thermal structure (e.g., Figure 1) is expressed as a function of time, it needs to be converted to a function of the distance from a ridge axis for Stoke flow calculation, by prescribing plate velocity. The aspect ratios of 4:1 and 8:1 corerspond to plate velocity of $\sim$39 km Ma^{-1} and $\sim$77 km Ma^{-1}, respectively. We found negligible differences among different aspect ratios, and our main results are based on the aspect ratio of 8:1. Third, in the real (compressible) mantle, both thermal expansivity and mantle density change with depth. Because our Stokes flow calculation is done with the incompressible fluid approximation, it may appear adequate to use surface values for these properties in the topography scale, in the same way that temperature in the incompressible fluid approximation corresponds to potential temperature. Using α of $3{\times}10^{-5}$ K^{-1}, ΔT of 1350 K, D of 2.9×10^6 m, ρ_m of 3300 kg m^{-3}, and ρ_w of 1000 kg m^{-3}, the topography scale is found to be $\sim 1.7 \times 10^5$ m. However, surface topography is a result of balancing vertical normal stress at the surface, originating in thermal buoyancy distributed over the whole mantle, and topographic load with surface density contrast, so it may be more appropriate to regard that α and ρ_m in the numerator of equation (13) refer to their mantle average values, whereas ρ_m in the denominator of equation (13) to its surface value. Because α and ρ_m vary with temperature and pressure in the opposite direction (e.g., Anderson, 1995; Katsura et al., 2009; Wolf et al., 2015), the deviation of the product $\alpha\rho_m$ from its surface value is limited, and we vary b_h from 1.7×10^5 to 2.0×10^5 m.

Finally, secular cooling also results in the temporal variation of crustal thickness; a potential temperature difference of 10 K, for example, corresponds to a crustal thickness difference of $\sim$630 m, according to the mantle melting model of Korenaga et al. (2002). Actually, the thickness and density of oceanic crust as well as those of depleted lithospheric mantle all vary with mantle potential temperature, so based on the parameterization of these variables by Korenaga (2006), we include their net effect on

isostasy in the subsidence equation as

$$d^3_{\mathrm{KK16}}(t) = d_0 + d_1 f_{\mathrm{TC}} \sqrt{t} + d_2 \tanh(e_2 t) + b_h (w_2^* - w_1^*) + \beta t \frac{dT_p}{dt}, \tag{14}$$

where β is 12 m K^{-1} and dT_p/dt denotes the rate of secular cooling. This linear dependence on potential temperature is valid only in the vicinity of mantle potential temperature of 1350 °C ($\pm$30 K).

In Figure 3a, we can see how incomplete viscous relaxation, radiogenic heating, and secular cooling reduce the original subsidence rate ($\sim$500 m Ma$^{-1/2}$). For a reference case, we use the internal heat production of 2.3×10^{-12} W kg^{-1}, the secular cooling rate of 100 K Ga^{-1}, the viscosity contrast between the upper and lower mantle of 10, the topography scale of 1.7×10^5 m, and f_{TC} of 0.85. For old seafloor (>100 Ma old), the effects of radiogenic heating and secular cooling are significant; at 150 Ma old seafloor, for example, the secular cooling of 100 K Ga^{-1} alone can lift seafloor by $\sim$800 m (Figure 3b). The reason for such a strong influence on subsidence, despite their seemingly minor influence on thermal structure, may be understood from the topography kernel (Parsons & Daly, 1983), which quantifies the sensitivity of surface topography to subsurface density structure. Figure 4 compares topography kernels corresponding to three different viscosity profiles, at wavelengths of 3000, 6000, and 12000 km. In general, a more viscous lower mantle reduces the sensitivity to deep-mantle density anomalies, whereas a longer wavelength leads to greater sensitivity. Thus, regardless of assumed viscosity structure, large-scale warming, such as expected from radiogenic heating and secular cooling, can add up to slowing down seafloor subsidence considerably and seems to have the potential to explain seafloor flattening.

The sensitivities of seafloor topography with respect to various factors are shown in Figure 5. Uncertainties associated with these factors correspond to similar uncertainties in predicted subsidence, suggesting that different combinations of model parameters can result in the same subsidence behavior. For example, the effect of a greater viscosity contrast between the upper and lower mantle would easily be compensated by a slight increase in the rate of secular cooling (Figure 5a,b). As explained in §2.3, we assume that thermal anomalies originating in radiogenic heating and secular cooling extend to the base of the mantle, and the effect of relaxing this assumption can be seen in Figure 5e. Because the topography kernels steadily decrease with increasing depth (Figure 4), truncating the bottom half of thermal anomalies results in only $\sim$25 % reduction, e.g., $\sim$300 m at 100 Ma. For comparison, the case of considering only the top 10% of mantle column (i.e., only the lithospheric part) is also shown in Figure 5e. As already shown by Korenaga and Kore-

naga (2016), neglecting the contribution of the deeper, sublithospheric part fails to explain even the subsidence of young seafloor.

This concludes our theoretical preparation, and we now turn to the global analysis of seafloor topography and heat flow, the result of which will be used to define a new reference model for the suboceanic mantle.

3 Global Data Analysis

We used the ETOPO1 bedrock data (Amante & Eakins, 2009) for global seafloor topography. The effect of sediment loading was taken into account using the empirical relation of Schroeder (1984) and the global sediment thickness database of Straume et al. (2019). Areas with sediment thickness larger than 2000 m are not considered in this study because sediment correction becomes inaccurate. To identify normal seafloor, we followed the procedure outlined by Korenaga and Korenaga (2008). First, residual depth anomaly with respect to the plate model of Stein and Stein (1992) is calculated, using the global seafloor age model of Seton et al. (2020). Second, to focus on large-scale anomalous regions associated with hotspot chains and oceanic plateaus, we apply a Gaussian filter of 150 km diameter to residual bathymetry; this filtering removes the influence of small seamounts in the subsequent steps. Then, we define areas with residual depth greater than 1 km as 'anomalous crust'. Finally, using the distance criterion of Korenaga and Korenaga (2008), the seafloor located more than 300 km from the anomalous regions is marked as normal seafloor (Figure 6a).

The above strategy of identifying normal seafloor is to remove the regions clearly influenced by the emplacement of anomalously thick crust such as hotspot islands and oceanic plateaus, which are commonly thought to result from the impingement of mantle plumes, i.e., external perturbations to the evolution of oceanic lithosphere. Our screening does not remove regions with positive dynamic topography uncorrelated with the emplacement of anomalously thick crust. We do not screen out regions covered by anomalously thin crust such as fracture zones, either. Anomalously thin crust at fracture zones result from the dynamics of melt migration (e.g., Tolstoy et al., 1993; Hooft et al., 2000), which would barely affect total melt volume produced by mantle upwelling, thus total crustal buoyancy on regional bathymetry. Anomalously thin crust can sometimes emerge at a slow spreading ridge, but a global compilation shows little correlation between crustal thickness and spreading rate (Christeson et al., 2019); crustal thickness variations at mid-ocean ridges are often associated with variations in mantle potential temperature (e.g., Klein, 2003; Holmes et al., 2008), which are internal to the evolution of the oceanic lithosphere. By using the sediment correction scheme of Hoggard et al. (2017), we could include heavily-sedimented pas-

sive margins in our analysis, but correcting for anomalously thick crust observed at volcanic rifted margins, as attempted by Hoggard et al. (2017), is deemed unreliable because the mantle process that is responsible for excess magmatism during continental breakup can lead to the anomalous density structure of crust as well as lithospheric mantle (e.g., Korenaga et al., 2001). Whether volcanic or nonvolcanic, passive margins are generally subject to the possibility of extensively stretched continental crust (e.g., Buck, 1991; Huismans & Beaumont, 2011; Geoffroy et al., 2015; Yuan et al., 2020), and we choose not to include data from heavily-sedimented passive margins.

For surface flow, we used the global ocean heat flow database compiled by Hasterok (2010). As in Hasterok et al. (2011), we first eliminated non-positive heat flow data. We further eliminated data that were not from the normal seafloor as defined above. This screening is more stringent than that used by Hasterok et al. (2011), which is based simply on the spatial extent of hotspots and oceanic plateaus as defined by Coffin and Eldholm (1994). Subsequent data screening and correction are basically the same as done by Hasterok et al. (2011) and Hasterok (2013): (1) heat flow data exceeding the prediction of the plate model of (Stein & Stein, 1992) by 2000 mW m^{-2} are removed; (2) to account for data compromised by hydrothermal circulation, heat flow data are removed when they are within 60 km of seamounts or with sediment thickness less than 400 m; (3) sedimentation correction is applied with a thermal diffusivity of 0.3×10^{-6} m^2 s^{-1} (Von Herzen & Uyeda, 1963). The only difference from the analysis of Hasterok et al. (2011) is that we do not restrict the second screening to seafloor age younger than 65 Ma ago, because even at seafloor older than 65 Ma ago, the effect of hydrothermal circulation persists where topographic variations are significant (e.g., Von Herzen, 2004; Fisher & Von Herzen, 2005). As in the previous studies (Hasterok et al., 2011; Hasterok, 2013), the distribution of screened heat flow data is highly uneven, clustering in a few locations such as the Atlantic passive margins, the equatorial Pacific, and the western Pacific margins (Figure 6b).

4 New Reference Model

The age-depth relation for normal seafloor, based on the global analysis described in the previous section, is shown in Figure 7a. Also shown is a prediction based on equation (14), with the internal heat production of 2.3×10^{-12} W kg^{-1}, the secular cooling rate of 100 K Ga^{-1}, the viscosity contrast between the upper and lower mantle of 10, the topography scale of 1.7×10^5 m, and f_{TC} of 0.85, and this prediction can explain the observed age-depth relation reasonably well; actually, this good fit to the observation is why we chose this particular case as a reference in Figures 3 and 5. Each of these chosen parameters, i.e., radiogenic heat production, secular cooling rate, viscosity contrast, topog-

raphy scale, and effective thermal expansivity, suffers from nontrivial uncertainty, but most importantly, it is relatively easy to explain the age-depth relation observed for all, not just the young part, of normal seafloor, in the framework of half-space cooling, without invoking sublithospheric convection. Even if some model parameters are different from their reference values, it is still possible to obtain a similar fit to data by varying other parameters within their uncertainties (Figure 7b).

We thus adopt our reference case as a new reference model for the depth of normal seafloor, which may be parameterized as:

$$d_{\mathrm{ref}}(t) = d_0 + d_1 f_{TC}\sqrt{t} + d_2 \tanh(e_2 t) + \sum_{n=1}^{4} p_n t^{n/2}, \tag{15}$$

where d_0=2600 m, d_1=409 m Ma$^{-1/2}$, f_{TC}=0.85, d_2=930 m, e_2=0.018 Ma^{-1}, p_1=32.85 Ma$^{-1/2}$, p_2=$-$18.39 Ma^{-1}, p_3=0.3023 Ma$^{-3/2}$, and p_4=$-$0.0054 Ma^{-2}. For comparison, predictions from the classic half-space cooling model of Carlson and Johnson (1994) and the plate model of Stein and Stein (1992) are also shown in Figure 7. The plate model of Stein and Stein (1992) was fit to the bathymetry of the North Pacific and Northwest Atlantic, without removing anomalously shallow regions such as hotspot islands and oceanic plateaus. As such, it tends to give slightly too shallow bathymetry when seafloor age is greater than $\sim$50 Ma old. Of course, one can still define a new plate model, by changing plate thickness, for example, to better fit the observed age-depth relation, but the merit of producing yet another model with a physically unrealistic boundary condition is unclear.

The age-heat flow relation for the normal seafloor is shown in Figure 8. Compared to the age-depth relation, this observation suffers from greater scatters, partly because of paucity of relevant data (section 3) and partly because marine heat flow data are susceptible to various factors including hydrothermal circulation associated with topographic variations (e.g., Nagihara et al., 1996; Hasterok et al., 2011) and lithospheric deformation (e.g., Yamano et al., 2014). Surface heat flow based on the modeling of Korenaga and Korenaga (2016), i.e., $q^0_{\mathrm{KK16}}(t)$ (equation (4)), is also shown, along with those based on the half-space cooling model (Lister, 1977) and the plate model (Stein & Stein, 1992). As repeatedly discussed in the literature (e.g., Lister et al., 1990; Jaupart & Mareschal, 2015), predictions from the classic half-space cooling model become too low for old seafloor, but our prediction, which is also based on half-space cooling, but with variable material properties, can fit the observation similarly well as the plate model, when the scatters of heat flow data are taken into account. As discussed in section 2.2, the effects of radiogenic heating and

secular cooling on surface heat flow are very minor, and we can incorporate them as:

$$\begin{aligned} q_{\text{ref}}(t) &= q^0_{\text{KK16}}(t)\frac{q_2(t)}{q_1(t)} \\ &= \frac{1}{\sqrt{t}}\left(1+\frac{2H\gamma t}{C_P\Delta T}+\frac{\delta T(t)}{\Delta T}\right)\sum_{n=0}^{4} c_n t^{n/2}, \end{aligned} \tag{16}$$

which is also shown in Figure 8. Here t is time in Ma, H=2.3 $\times$ 10^{-12} W kg^{-1}, γ=3.154 $\times$ 10^{13} s Ma^{-1} (the number of seconds in Ma), C_P=1200 J K^{-1} kg^{-1}, ΔT=1350 K, $\delta T(t)$ varies linearly from 0 at present to 20 K at 200 Ma, c_0 = 338.4, c_1 = 66.7, c_2 = -8.26, c_3 = 0.53, and c_4 = -0.013.

Because our new reference models for seafloor depth and surface heat flow both satisfy observations in a satisfactory manner, we can settle on the reference thermal structure as

$$T_{\text{ref}}(t,z) = T^0_{\text{KK16}}(t,z)\frac{T_2(t)}{T_1(t)}. \tag{17}$$

The expressions for T^0_{KK16}, T_1, and T_2 are given in equations (2), (6), and (7), respectively, and for the calculation of T_1 and T_2, we use the same values of H, C_P, and $\delta T(t)$ used for $q_{\text{ref}}(t)$, along with κ of 10^{-6} m^2 s^{-1}. This new reference thermal structure is compared with those based on the traditional half-space cooling and plate models in Figure 9. They are also compared in terms of geotherms at 50, 100, and 150 Ma. Mostly because of low thermal conductivity used for oceanic crust, the new reference model is hotter than the traditional half-space model, though it is still colder than the plate model at shallow depths (shallower than $\sim$200 km). Because of radiogenic heating and secular cooling, however, the new model is slightly hotter than the plate model for the rest of the mantle, and this difference is sufficient to explain the topography of normal seafloor.

5 Discussion

5.1 Surface Wave Tomography

Reference models for the evolution of oceanic lithosphere have usually been constrained by surface observables only, and this is also the case for our new reference model. Here surface observables such as seafloor topography and heat flow are used as proxies to the thermal structure of the oceanic mantle. Gravity and geoid are also surface observables, but their utilities in distinguishing between different reference models have been limited. Weak geoid contrasts at fracture zones, for example, were once interpreted to support the plate model (Richardson et al., 1995), but this interpretation turns out to be based on the incorrect theoretical calculation of geoid anomalies (Cadio & Korenaga, 2012). The half-space cooling and plate models do predict different isostatic geoid anoma-

677 lies, but the difference between them is too small to be diagnostic, in the presence of
678 other perturbations expected in the geoid (Hager, 1983). As shallower anomalies have a greater
679 influence on a surface potential field, the analysis of Hager (1983) may serve as an upper bound
680 on differences among reference models in an isostatic geoid; density anomalies in our new ref-
681 erence model are more broadly distributed along mantle depths than the plate model.

682 Because the thermal structure is the primary element of any reference model, its
683 validity may be assessed more directly by seismological means. The resolution of surface
684 wave tomography has been steadily improving, and tomographic models may provide an
685 insight for suboceanic thermal structure (e.g., Ritzwoller et al., 2004; Maggi et al., 2006;
686 Priestley & McKenzie, 2013). Here we use recent high-resolution tomography models
687 (SEMum2 of French et al. (2013), SL2013 of Schaeffer and Lebedev (2013), 3D2018 of
688 Debayle et al. (2016), and PAC-age of Isse et al. (2019)) to compare with the thermal
689 structure of our reference model: the first model is based on the full-waveform inversion
690 for global data set, and the latter three on multi-mode Rayleigh wave dispersion measure-
691 ments including data from high-density regional temporal networks. Among them, PAC-
692 age of Isse et al. (2019) is unique in a sense that it covers only the Pacific Ocean region and
693 employs data from nearly 200 stations of broadband ocean bottom seismometer (BBOBS) ar-
694 rays together with those from circum-Pacific land-stations.

695 Figure 10 shows the shear velocity (β_V; the velocity of a vertically polarized
696 horizontally propagating shear wave) structure of the suboceanic mantle as a function of
697 seafloor age. Figures 10a-d are based on age stacking using all seafloor with known ages,
698 whereas Figures 10e-h are restricted to normal seafloor (Figure 6a). The quality of this
699 age stacking is not uniform as the number of data used varies considerably across seafloor
700 age (Figure 10i). For the all seafloor cases, for example, the average seismic structure for
701 seafloor older than $\sim$100 Ma ago is supported by only half as much data as that for
702 younger seafloor. The situation is more severe for age stacking with normal seafloor; the
703 number of relevant data drops sharply at $\sim$40 Ma and becomes marginal at $>$100 Ma ago.
704 This is expected because it is more difficult to find normal seafloor as the seafloor be-
705 comes older (Heestand & Crough, 1981; Davies, 1988a; Korenaga & Korenaga, 2008). It should
706 also be noted that waveform inversion approach of SEMum2 tends to resolve strong veloc-
707 ity anomaly, especially low velocity ones, as it tries to fit amplitude as well as phase.

708 The thermal structure of our new reference model is also shown up to 1200 °C. For
709 the all seafloor cases, a reasonable match between the thermal structure and the variation
710 of seismic velocity can be seen up to the isothermal contour of 1100 or 1200 °C. This
711 direct comparison of isothermal and isotach contours is meaningful up to $\sim$1100 °C; at
712 higher temperatures, the comparison becomes more difficult because the effect of attenua-

tion becomes important, but how to incorporate such an effect is model-dependent (e.g., Goes et al., 2012). The PAC-age model is notable in that its normal-seafloor age stack (Figure 10h) indicates a more steady growth of oceanic lithosphere than its all-seafloor age stack (Figure 10d). With other models, age stacks on all seafloor and normal seafloor both appear to suggest some substantial perturbations to lithospheric growth. Reduced perturbations in a normal-seafloor age stack is what we expect from our definition of normal seafloor, and the normal-seafloor age stack of PAC-age may benefit from a better regional coverage with BBOBS data. As PAC-age is only for the Pacific Ocean, similar figures just for the region are also made (Figure S4); differences among normal-seafloor age stacks are amplified for this regional stack. The number of data used for age stack on old normal seafloor is highly limited, and these differences indicate that recent tomographic models still do not agree well on small-scale features.

Here we have restricted ourselves to the lithospheric part of the tomographic models. As mentioned above, examining the deeper part of those models is more difficult because correcting for the effect of attenuation is model-dependent. Richards et al. (2020), for example, used the anelastic parameterization of Yamauchi and Takei (2016) to compare half-space cooling and plate models against SL2013, SEMum2, and one more tomographic model (CAM2016; Ho et al., 2016); their results seem to indicate that SEMum2 and CAM2016 are consistent with half-space cooling and plate models, respectively, and SL2013 is somewhere in-between. Richards et al. (2020), however, calibrated the anelastic parameters for each of these different tomographic models, and some of the calibrated parameters vary substantially among models (see their Table F.3). This is equivalent to assuming different versions of viscoelasticity for different tomographic models, suggesting considerable incompatibilities among those published tomographic images with respect to the lithosphere-asthenosphere system.

In order to further advance our understanding of the evolution of the suboceanic mantle, it is essential that we improve the coverage of seismic networks in the ocean. Temporal deployment of a BBOBS array now allows us to constrain the regional 1-D seismic depth profile (including seismic anisotropy) of the entire lithosphere-asthenosphere system. For example, Takeo et al. (2018) recently resolved the regional average 1-D β_V structure beneath two BBOBS-array sites (beneath 130 Ma and 140 Ma old normal seafloor in the northwestern Pacific), and reported that the observed structural difference at two sites with similar ages cannot be attributed to the conductive cooling effect alone and that a secondary process other than simple cooling of the lithosphere (either half-space cooling or plate-model like cooling), such as a small-scale convection, was necessary. Accumulation of such observations by a large number of BBOBS arrays (e.g., Kawakatsu & Utada,

2017) and their incorporation in large-scale tomography models would drastically increase our understanding of the plate tectonic evolution of the cooling Earth. The new reference model presented here, combined with the theoretical and experimental mineralogical framework (e.g., Stixrude & Lithgow-Bertelloni, 2005), will provide a reference velocity model that can be directly compared with regional 1-D observations and tomography to unravel the dynamic states of the Earth.

5.2 Some Remarks on Previous Reference Models

The plate model has long been popular in the literature (e.g., McKenzie, 1967; Parsons & Sclater, 1977; Stein & Stein, 1992; Hillier & Watts, 2005; Hasterok, 2013; Richards et al., 2018), primarily because it explains depth and heat flow data for old seafloor reasonably well. It was originally proposed to explain nearly constant heat flow on old seafloor (Langseth et al., 1966; McKenzie, 1967), but it can explain the age-depth relation as well. The success of the plate model in explaining these surface observables owes, however, entirely to the use of an artificial boundary condition at the bottom, which comprises of two free parameters, plate thickness and basal temperature. There is no such a boundary in the real mantle with a constant temperature, but these free parameters allow the plate model to be flexible enough to fit observations on older seafloor.

One persistent thread in the previous plate models is to refine the quality of observations to be fit. Initially, Parsons and Sclater (1977) used both bathymetry and heat flow data in the North Pacific and the North Atlantic to find a plate thickness of 125 km and a basal temperature of 1350 °C. Stein and Stein (1992) also used both kinds of data in the North Pacific and the Northwest Atlantic but in a greater quantity and derived a plate thickness of 95 km and a basal temperature of 1450 °C. Obviously, these two models represent very different thermal structures, and subsequent plate models fluctuate around these two. For example, Hillier and Watts (2005) tried to remove the effect of hotspots, seamounts, and oceanic plateaus in the North Pacific by a semi-quantitative method and derived a plate thickness of 120 km and a basal temperature of 1363 °C. On the other hand, Crosby et al. (2006) used near-zero gravity anomalies to identify normal seafloor and obtained a plate thickness of 90 km. Hasterok (2013) also arrived at the same plate thickness, using a global compilation of heat flow data, and for basal temperature, he adopted the petrological estimate of 1300-1400 °C (Herzberg et al., 2007). Goutorbe and Hillier (2013) jointly fit depth, heat flow, and thermal structure derived from surface wave tomography and obtained a plate thickness of 106 km and a basal temperature of 1390 °C. More recently, on the basis of basement depth and heat flow data, Richards et al. (2018) derived a plate thickness of

135 km and a potential temperature of 1300 °C (which is equivalent to a basal temperature of 1360 °C), which are similar to the values adopted by Parsons and Sclater (1977).

A reference model for the evolution of oceanic lithosphere should focus on the intrinsic component of evolution, i.e., excluding external perturbations such as brought by the emplacement of hotspot islands, seamounts, and oceanic plateaus. Otherwise, it is impossible to use a reference model to quantify the influence of such excess magmatism on the evolution of oceanic lithosphere. To build a reference model, therefore, it is important to identify the 'normal part of seafloor first (e.g., Korenaga & Korenaga, 2008), though this issue has not received adequate care in the various plate models mentioned above. For example, Parsons and Sclater (1977) and Stein and Stein (1992) did not exclude anomalous crustal regions at all. Later studies made some efforts, though screening criteria adopted are either qualitative or quantitative but unreliable. The method developed by Hillier and Watts (2005) to remove anomalous regions is essentially an automation of visual inspection. The use of zero gravity anomaly to identify normal seafloor (Crosby et al., 2006) is difficult to justify because zero gravity anomaly could only mean isostasy; anomalous crustal regions can attain isostasy and has no gravity anomalies (e.g., Ontong Java Plateau). The use of surface wave tomography as additional observational constraints (Goutorbe & Hillier, 2013) is likely to be premature (section 5.1). Basement depth data used by Richards et al. (2018), which were originally compiled by Hoggard et al. (2017), do not suffer from the uncertainty of sediment correction, but their localities are biased to continental margins (see Figure 1 of Hoggard et al. (2017)). As mentioned in §3, crustal structures at rifted continental margins, whether volcanic or nonvolcanic, are variably affected by the uniqueness of mantle melting and crustal accretion processes during continental breakup (e.g., White & McKenzie, 1989; Kelemen & Holbrook, 1995; Holbrook et al., 2001; Korenaga et al., 2002; Van Avendonk et al., 2006; White et al., 2008; Minshull, 2009) as well as the possibility of extensively stretched continental crust (e.g., Buck, 1991; Huismans & Beaumont, 2011; Geoffroy et al., 2015; Yuan et al., 2020).

Some authors attempted to improve the plate model by using more accurate mineral physics data. For example, Honda and Yuen (2001) used temperature-dependent thermal conductivity, and McKenzie et al. (2005) incorporated a radiative contribution to thermal conductivity. Grose and Afonso (2013) considered temperature- and pressure-dependent material properties, including thermal conductivity, heat capacity, and density, and showed that the importance of crustal insulation effect. Such intricate care of material properties in the plate model is, however, compromised by the use of the artificial bottom boundary condition; the bottom boundary condition starts to dictate the growth of a thermal boundary layer as soon as the boundary layer grows thicker than the assumed plate thickness,

819 which can take place at the seafloor as young as 30 Ma ago (see Figure 4c of (Korenaga
820 & Korenaga, 2016)). The use of the plate model thus affects the thermal evolution of young
821 oceanic lithosphere as well. Those who favor the plate model may defend their bottom bound-
822 ary condition as being an approximation for the effect of small-scale convection (e.g., Parsons
823 & McKenzie, 1978), but this argument implies that small-scale convection, which could take
824 place beneath old seafloor, exerts an acausal effect on the mantle beneath young seafloor (Korenaga,
825 2020). In addition, it is not yet known how well small-scale convection with realistic mantle
826 rheology is approximated by the plate model, as discussed next.

827 ### 5.3 Role of Small-Scale Convection and Nature of Secular Cooling

828 Our new reference model is built without the dynamics of small-scale convection,
829 but its success of explaining the observed seafloor depth and heat flow (Figures 7 and 8)
830 does not necessarily rule out the occurrence of small-scale convection beneath the normal
831 seafloor of any age. Whereas the new reference model does match the overall trend of the
832 age-depth relation, actual data start to oscillate around the new reference model, for
833 seafloor older than $\sim$100 Ma old (Figure 7); most of depth data plot lower than the new
834 reference model from $\sim$110 to $\sim$120 Ma old, higher from $\sim$120 to $\sim$130 Ma old, and
835 then lower again after that. Though such an oscillation may result from the paucity of
836 normal seafloor with old ages or from the incompleteness of filtering out anomalous
837 regions, it is possible that they reflect the perturbations to the lithospheric structure by
838 small-scale convection.

839 In Figure 11, three different thermal models are compared, the plate model, the half-
840 space cooling model with radiogenic heating and secular cooling (equation 7), and the
841 half-space cooling model with radiogenic heating, secular cooling, and small-scale convec-
842 tion. The last one is prepared following the procedure outlined by Korenaga (2015); the
843 results of a 2-D ridge-parallel model with internal heat production are horizontally aver-
844 aged to generate a ridge-perpendicular cross section. The convection simulation was con-
845 ducted using the internal Rayleigh number of $10^{9.4}$ (corresponding to the asthenospheric
846 viscosity of $\sim 10^{19}$ Pa s) and the Frank-Kamenetskii parameter of 18 (corresponding to the
847 activation energy of $\sim$300 kJ mol^{-1}). With this combination of asthenospheric viscosity
848 and the temperature-dependent viscosity, small-scale convection starts to take place when
849 seafloor age reaches $\sim$60 Ma and slows down the conductive thickening of lithosphere. Ow-
850 ing to the realistically high temperature dependence of viscosity, the convective delamination
851 of lithosphere is limited to its lowermost portion (with potential temperatures from $\sim$1200-
852 1350 °C; see Figure 8 of Korenaga (2015)). As such, the upper half of oceanic lithosphere
853 is only weakly influenced by small-scale convection, so surface heat flux is barely affected (Korenaga,

2009). On the other hand, the delamination of lithosphere is immediately reflected in surface topography. By comparing Figures 11b and 11c, oceanic lithosphere is thinned by $\sim$50 km by small-scale convection, with the temperature contrast of $\sim$200 K. A simple isostasy calculation indicates that such thinning results in seafloor shallowing of $\sim$400 m, which is comparable to the amplitude of fluctuations around the new reference model (Figure 7).

One important complication for the physics of small-scale convection is that real mantle rheology includes both diffusion creep and dislocation creep (e.g., Karato & Wu, 1993; Hirth & Kohlstedt, 2003). Being non-Newtonian rheology, the onset of convection with dislocation creep requires finite-amplitude stress (e.g., Solomatov & Barr, 2007), so it would not take place in isolation. One possible path to activate dislocation creep in small-scale convection is to first develop small-scale convection with diffusion creep only and raise the stress level. As mentioned in §2.3, the low Frank-Kamenetskii parameter used for Figure 2 (θ=6 or the activation energy of $\sim$100 kJ mol^{-1}) is usually considered to be too low to be compatible with the rock mechanics of olivine aggregates, but such a low activation energy has been suggested from the occurrence of possible small-scale convection beneath fracture zones (Cadio & Korenaga, 2016), where horizontal thermal gradients may be high enough to enhance convective stress. The development of small-scale convection is governed by the interaction between diffusion and dislocation creep, and modeling the onset of convection with such composite rheology requires an accurate understanding of upper mantle rheology. Given uncertainties associated with the analysis of rock deformation data (see section 3 of Korenaga (2020) for a review), we would need to test a range of possibilities for composite rheology (e.g., different combinations of activation energies and volumes of diffusion and dislocation creep). Small-scale convection is likely to take place beneath mature oceanic lithosphere, but this difficulty with composite rheology prevents us to be more specific about its details.

By comparing Figure 11a and 11c, it is evident that the bottom boundary condition of the plate model is too crude an approximation to the effect of small-scale convection. The thermal structure of shallow oceanic lithosphere is similar between them, but the structure of the deeper lithosphere, which becomes important when discussing the lithosphere-asthenosphere boundary, is substantially different. If the temperature dependence of mantle viscosity is as high as rock mechanics suggests, small-scale convection cannot maintain a constant plate thickness because only a small portion of lithosphere can delaminate. Obviously, if we want to find an observational support for the occurrence of small-scale convection by, for example, some seismological means, it is better to use a half-space cooling model (e.g., Figure 11b) as a reference. If we instead use the plate

model as a reference, we would not be able to properly constrain the nature of small-scale convection.

When using our reference model to quantify the extent of small-scale convection, it is important to recognize that deviations from our reference thermal structure can be caused not only by small-scale convection, but also by the spatially heterogeneous nature of secular cooling. This is because, unlike radiogenic heating, the notion of secular cooling is valid only on a global average (§2.3). According to petrological estimates (Herzberg et al., 2010), Earth is cooling at the rate of $\sim$100-150 K Ga^{-1} for the past 1 Ga, but this secular cooling is achieved primarily through the subduction of cold oceanic lithosphere, and it takes finite time for this localized cooling to propagate on a global scale. Thus, when the mantle currently beneath 100 Ma-old seafloor was at mid-ocean ridges 100 Ma ago, for example, it is expected to be hotter by $\sim$10-15 K than the mantle beneath current mid-ocean ridges *on average*; it can have different temperatures regionally, even in the absence of small-scale convection. By the same token, the mantle beneath mid-ocean ridge does not have to possess the same potential temperature globally, and indeed it does not; even after excluding the likely influence of hotspots, along-ridge variations in the mantle potential temperature seem to have an amplitude of about 50 K (e.g., Klein & Langmuir, 1987; Dalton et al., 2014). The new reference model, if combined with future developments in the physics of small-scale convection, has the potential of resolving how secular cooling has actually been taking place in the convecting mantle.

6 Summary

We have developed a new reference model for the evolution of oceanic lithosphere, which can explain both bathymetry and heat flow of the normal seafloor. Unlike the plate model, it does not employ an unphysical boundary condition, but it does not invoke small-scale convection either. We are able to show that, even without calling for the operation of small-scale convection, it is possible to explain the overall feature of seafloor topography and heat flow, if we consider the processes that must be taking place ubiquitously beneath seafloor, i.e., incomplete viscous relaxation, radiogenic heating, and secular cooling. In particular, the effect of secular cooling on the depths of old seafloor is quite substantial (Figure 3b). Even though the amplitude of temperature variations associated with secular cooling is small, the deep sensitivity of long-wavelength topographic kernels means that such minute temperature variations can have substantial cumulative effects on bathymetry. Earth has been cooling down, because surface heat flux is not balanced with internal heat production, and this fact has long been known from the thermal budget of the present-day Earth (e.g., Christensen, 1985; Korenaga, 2008; Jaupart et al., 2015) as well as from petrological estimates

on the cooling history of the upper mantle (e.g., Abbott et al., 1994; Herzberg et al., 2010). Our reference model is the first reference model that quantifies the consequence of this well-known fact on the evolution of oceanic lithosphere.

Our model is built on conductive cooling with variable material properties as well as instantaneous Stokes flow calculations, and the results of relevant numerical modeling are parameterized so that the new reference model can easily be computed, without conducting any geodynamical modeling. As our model is fit to explain the normal seafloor, it will be useful to better quantify the impact of the emplacement of hotspot islands and oceanic plateaus. It will also help better understand the effect of small-scale convection and the regional history of secular cooling in the convecting mantle.

Acknowledgments

This work is theoretical in nature, and the data on which this article is based are available in Seton et al. (2020), Hasterok (2010), Straume et al. (2019), French et al. (2013), Schaeffer and Lebedev (2013), Debayle et al. (2016), and Isse et al. (2019). MATLAB and Python codes to calculate the new reference model are available at `https://github.com/jun-korenaga/prom1`. The authors thank Hisashi Utada for stimulating discussion. Reviews from two anonymous referees were helpful to improve the clarity and accuracy of the manuscript. This work was sponsored in part by the U.S. National Science Foundation under grant EAR-1753916.

References

Abbott, D., Burgess, L., Longhi, J., & Smith, W. H. F. (1994). An empirical thermal history of the Earth's upper mantle. *J. Geophys. Res.*, *99*, 13835-13850.

Amante, C., & Eakins, B. W. (2009). *ETOPO1 1 arc-minute global relief model: Procedures, data sources and analysis* (Tech. Rep.). Boulder, CO: NOAA.

Anderson, O. L. (1995). *Equations of State for Solids in Geophysics and Ceramic Science*. Oxford Univ. Press.

Aulbach, S., & Arndt, N. T. (2019). Eclogites as paleodynamic archives: Evidence for warm (not hot) and depleted (but heterogeneous) Archaean ambient mantle. *Earth Planet. Sci. Lett.*, *505*, 162-172.

Buck, W. R. (1991). Modes of continental lithospheric extension. *J. Geophys. Res.*, *96*, 20161-20178.

Cadio, C., & Korenaga, J. (2012). Localization of geoid anomalies and the evolution of oceanic lithosphere: A case study from the Mendocino Fracture Zone. *J. Geophys. Res.*, *117*, B10404, doi:10.1029/2012JB009524.

Cadio, C., & Korenaga, J. (2016). Macroscopic strength of oceanic lithosphere revealed by ubiquitous fracture-zone instabilities. *Earth Planet. Sci. Lett.*, *449*, 295-301.

Carlson, R. L., & Johnson, H. P. (1994). On modeling the thermal evolution of the oceanic upper mantle: An assessment of the cooling model. *J. Geophys. Res.*, *99*, 3201-3214.

Carslaw, H. S., & Jaeger, J. C. (1959). *Conduction of Heat in Solids, 2nd ed.* Oxford Univ. Press.

Chesley, C., Key, K., Constable, S., Behrens, J., & MacGregor, L. (2019). Crustal cracks and frozen flow in oceanic lithosphere inferred from electrial anisotropy. *Geochem. Geophys. Geosys.*, *20*, 5979-5999.

Christensen, U. R. (1985). Thermal evolution models for the Earth. *J. Geophys. Res.*, *90*, 2995-3007.

Christeson, G. L., Goff, J. A., & Reece, R. S. (2019). Synthesis of oceanic crustal structure from two-dimensional seismic profiles. *Rev. Geophys.*, *57*, 504-529, https://doi.org/10.1029/2019RG000641.

Coffin, M. F., & Eldholm, O. (1994). Large igneous provinces: Crustal structure, dimensions, and external consequences. *Rev. Geophys.*, *32*, 1-36.

Coltice, N., Phillips, B. R., Bertrand, H., Ricard, Y., & Rey, P. (2007). Global warming of the mantle at the origin of flood basalts over supercontinents. *Geology*, *35*, 391-394.

Crosby, A. G., McKenzie, D., & Sclater, J. G. (2006). The relationship between depth, age and gravity in the oceans. *Geophys. J. Int.*, *166*, 443-573.

Crough, S. T. (1977). Approximate solutions for the formation of the lithosphere. *Phys. Earth Planet. Inter.*, *14*, 365-377.

Dalton, C. A., Langmuir, C. H., & Gale, A. (2014). Geophysical and geochemical evidence for deep temperature variations beneath mid-ocean ridges. *Science*, *344*, 80-83.

Davaille, A., & Jaupart, C. (1994). Onset of thermal convection in fluids with temperature-dependent viscosity: Application to the oceanic mantle. *J. Geophys. Res.*, *99*, 19853-19866.

Davies, G. F. (1988a). Ocean bathymetry and mantle convection: 1. large-scale flow and hotspots. *J. Geophys. Res.*, *93*, 10467-10480.

Davies, G. F. (1988b). Role of the lithosphere in mantle convection. *J. Geophys. Res.*, *93*, 10451-10466.

Davies, J. H., & von Blanckenburg, F. (1995). Slab breakoff: A model of lithosphere detachment and its test in the magmatism and deformation of collisional orogens. *Earth Planet. Sci. Lett.*, *129*, 85-102.

Davis, E. E., & Lister, C. R. B. (1974). Fundamentals of ridge crest topography. *Earth Planet. Sci. Lett.*, *21*, 405-413.

Debayle, E., Dubuffet, F., & Durand, S. (2016). An automatically updated S-wave model of

the upper mantle and the depth extent of azimuthal anisotropy. *Geophys. Res. Lett.*, *43*, 674-682.

Fisher, A. T., & Von Herzen, R. P. (2005). Models of hydrothermal circulation within 106 Ma seafloor: Constraints on the vigor of fluid circulation and crustal properties, below the Madeira Abyssal Plain. *Geochem. Geophys. Geosys.*, *6*, Q11001, doi:10.1029/2005gc001013.

Flament, N., Coltice, N., & Rey, P. F. (2008). A case for late-Archaean continental emergence from thermal evolution models and hypsometry. *Earth Planet. Sci. Lett.*, *275*, 326-336.

Forsyth, D. W. (1977). The evolution of the upper mantle beneath mid-ocean ridges. *Tectonophysics*, *38*, 89-118.

Forte, A. M., Simmons, N. A., & Grand, S. P. (2015). Constraints on seismic models from other disciplines — constraints on 3-D seismic models from global geodynamic observables: Implications for the global mantle convective flow. In *Treatise on Geophysics, 2nd ed.* (Vol. 1, p. 853-907). Elsevier.

French, S. W., Lekic, V., & Romanowicz, B. A. (2013). Waveform tomography reveals channeled flow at the base of the oceanic asthenosphere. *Science*, *342*, 227-230.

Galer, S. J. G. (1991). Interrelationships between continental freeboard, tectonics and mantle temperature. *Earth Planet. Sci. Lett.*, *105*, 214-228.

Geoffroy, L., Burov, E. B., & Werner, P. (2015). Volcanic passive margins: another way to break up continents. *Sci. Rep.*, *5*, 14828, doi:10.1038/srep14828.

Goes, S., Armitage, J., Harmon, N., Smith, H., & Huismans, R. (2012). Low seismic velocities below mid-ocean ridges: Attenuation versus melt retention. *J. Geophys. Res.*, *117*, B12403, doi:10.1029/2012JB009637.

Goutorbe, B., & Hillier, J. K. (2013). An integration to optimally constrain the thermal structure of oceanic lithosphere. *J. Geophys. Res.*, *118*, 432-446, doi:10.1029/2012JB009527.

Grose, C. J., & Afonso, J. C. (2013). Comprehensive plate models for the thermal evolution of oceanic lithosphere. *Geochem. Geophys. Geosys.*, *14*, 3751-3778, doi:10.1002/ggge.20232.

Guo, M., & Korenaga, J. (2020). Argon constraints on the early growth of felsic continental crust. *Sci. Adv.*, *6*, eaaz6234.

Hager, B. H. (1983). Global isostatic geoid anomalies for plate and boundary layer models of the lithosphere. *Earth Planet. Sci. Lett.*, *63*, 97-109.

Hager, B. H., & O'Connell, R. J. (1981). A simple global model of plate dynamics and mantle convection. *J. Geophys. Res.*, *86*, 4843-4867.

Harrison, C. G. A. (1999). Constraints on ocean volume change since the Archean. *Geophys.*

Res. Lett., *26*, 1913-1916.

Hasterok, D. (2013). A heat flow based cooling model for tectonic plates. *Earth Planet. Sci. Lett.*, *361*, 34-43.

Hasterok, D., Chapman, D. S., & Davis, E. E. (2011). Oceanic heat flow: Implications for global heat loss. *Earth Planet. Sci. Lett.*, *311*, 386-395.

Hasterok, D. P. (2010). *Thermal state of continental and oceanic lithosphere* (Unpublished doctoral dissertation). University of Utah.

Heestand, R. L., & Crough, S. T. (1981). The effect of hot spots on the oceanic age-depth relation. *J. Geophys. Res.*, *86*, 6107-6114.

Helffrich, G. R., & Wood, B. J. (2001). The Earth's mantle. *Nature*, *412*, 501-507.

Herzberg, C. (2019). Origin of high-Mg bimineralic eclogite xenoliths in kimberlite: A comment on a paper by Aulbach and Arndt (2019). *Earth Planet. Sci. Lett.*, *510*, 231-233.

Herzberg, C., Asimow, P. D., Arndt, N., Niu, Y., Lesher, C. M., Fitton, J. G., ... Saunders, A. D. (2007). Temperatures in ambient mantle and plumes: Constraints from basalts, picrites, and komatiites. *Geochem. Geophys. Geosys.*, *8*(2), Q02206, doi:10.1029/2006GC001390.

Herzberg, C., Condie, K., & Korenaga, J. (2010). Thermal evolution of the Earth and its petrological expression. *Earth Planet. Sci. Lett.*, *292*, 79-88.

Hillier, J. K., & Watts, A. B. (2005). Relationship between depth and age in the North Pacific ocean. *J. Geophys. Res.*, *110*, B02405, doi:10.1029/2004JB003406.

Hirth, G., & Kohlstedt, D. (2003). Rheology of the upper mantle and the mantle wedge: A view from the experimentalists. In J. Eiler (Ed.), *Inside the Subduction Factory* (p. 83-105). Washington, DC: American Geophysical Union.

Ho, T., Priestley, K., & Deloule, E. (2016). A global horizontal shear velocity model of the upper mantle from multimode Love wave measurements. *Geophys. J. Int.*, *207*, 542-561.

Hoggard, M. J., Winterbourne, J., Czarnota, K., & White, N. (2017). Oceanic residual depth measurements, the plate cooling model, and global dynamic topography. *J. Geophys. Res. Solid Earth*, *122*, 2328-2372, doi:10.1002/2016JB013457.

Holbrook, W. S., Larsen, H. C., Korenaga, J., Dahl-Jensen, T., Reid, I. D., Kelemen, P. B., ... Detrick, R. S. (2001). Mantle thermal structure and melting processes during continental breakup in the North Atlantic. *Earth Planet. Sci. Lett.*, *190*, 251-266.

Holmes, R. C., Tolstoy, M., Cochran, J. R., & Floyd, J. S. (2008). Crustal thickness variations along the Southeast Indian Ridge (100°–116°E) from 2-D body wave tomography. *Geochem. Geophys. Geosys.*, *9*, Q12020, doi:10.1029/2008GC002152.

Honda, S., & Yuen, D. A. (2001). Interplay of variable thermal conductivity and expansivity on the thermal structure of oceanic lithosphere. *Geophys. Res. Lett.*, *28*(2), 351-354.

Hooft, E. E. E., Detrick, R. S., Toomey, D. R., Collins, J. A., & Lin, J. (2000). Crustal thickness and structure along three contrasting spreading segments of the Mid-Atlantic Ridge, 33.5°-35°N. *J. Geophys. Res.*, *105*, 8205-8225.

Huang, J., Niu, F., Gordon, R. G., & Cui, C. (2015). Accurate focal depth determination of oceanic earthquakes using water-column reverberation and some implications for the shrinking plate hypothesis. *Earth Planet. Sci. Lett.*, *432*, 133-141.

Huang, J., & Zhong, S. (2005). Sublithospheric small-scale convection and its implications for residual topography at old ocean basins and the plate model. *J. Geophys. Res.*, *110*, B05404, 10.1029/2004JB003153.

Huang, J., Zhong, S., & van Hunen, J. (2003). Controls on sublithospheric small-scale convection. *J. Geophys. Res.*, *108*(B8), 2405, doi:10.1029/2003JB002456.

Huismans, R., & Beaumont, C. (2011). Depth-dependent extension, two-stage breakup and cratonic underplating at rifted margins. *Nature*, *473*, 74-78.

Isse, T., Kawakatsu, H., Yoshizawa, K., Takeo, A., Shiobara, H., Sugioka, H., ... Reymond, D. (2019). Surface wave tomography for the Pacific Ocean incorporating seafloor seismic observations and plate thermal evolution. *Earth Planet. Sci. Lett.*, *510*, 116-130.

Ito, G., & Mahoney, J. J. (2005). Flow and melting of a heterogeneous mantle: 2. implications for a chemically nonlayered mantle. *Earth Planet. Sci. Lett.*, *230*, 47-63.

Jain, C., Korenaga, J., & Karato, S. (2019). Global analysis of experimental data on the rheology of olivine aggregates. *J. Geophys. Res. Solid Earth*, *124*, 310-334, https://doi.org/10.1029/2018JB016558.

Jarvis, G. T., & Peltier, W. R. (1982). Mantle convection as a boundary layer phenomenon. *Geophys. J. R. Astron. Soc.*, *68*, 389-427.

Jaupart, C., Labrosse, S., Lucazeau, F., & Mareschal, J.-C. (2015). Temperatures, heat, and energy in the mantle of the Earth. In *Treatise on Geophysics, 2nd ed.* (p. 223-270). Elsevier.

Jaupart, C., & Mareschal, J.-C. (2015). Heat flow and thermal structure of the lithosphere. In *Treatise on Geophysics, 2nd ed.* (Vol. 6, p. 217-253). Elsevier.

Jochum, K. P., Hofmann, A. W., Ito, E., Seufert, H. M., & White, W. M. (1983). K, U and Th in mid-ocean ridge basalt glasses and heat production, K/U and K/Rb in the mantle. *Nature*, *306*, 431-436.

Karato, S. (2008). *Deformation of earth materials: Introduction to the rheology of the solid earth*. New York: Cambridge.

Karato, S., & Wu, P. (1993). Rheology of the upper mantle: A synthesis. *Science*, *260*, 771-778.

Katsura, T., Shatskiy, A., Manthilake, M. A. G. M., Zhai, S., Fukui, H., Yamazaki, D., ... Funakoshi, K. (2009). Thermal expansion of forsterite at high pressures determined

by in situ X-ray diffraction: The adiabatic geotherm in the upper mantle. *Phys. Earth Planet. Inter.*, *174*, 86-92.

Kawakatsu, H., Kumar, P., Takei, Y., Shinohara, M., Kanazawa, T., Araki, E., & Suyehiro, K. (2009). Seismic evidence for sharp lithosphere-asthenosphere boundaries of oceanic plates. *Science*, *324*, 499-502.

Kawakatsu, H., & Utada, H. (2017). Seismic and electrical signatures of the lithosphere-asthenosphere system of the normal oceanic mantle. *Annu. Rev. Earth Planet. Sci.*, *45*, 139-167.

Kelemen, P. B., & Holbrook, W. S. (1995). Origin of thick, high-velocity igneous crust along the U.S. East Coast Margin. *J. Geophys. Res.*, *100*, 10077-10094.

Klein, E. M. (2003). Geochemistry of the igneous oceanic crust. In *Treatise on geochemistry* (Vol. 3, p. 433-463). Elsevier.

Klein, E. M., & Langmuir, C. H. (1987). Global correlations of ocean ridge basalt chemistry with axial depth and crustal thickness. *J. Geophys. Res.*, *92*, 8089-8115.

Korenaga, J. (2006). Archean geodynamics and the thermal evolution of Earth. In K. Benn, J.-C. Mareschal, & K. Condie (Eds.), *Archean geodynamics and environments* (p. 7-32). Washington, D.C.: American Geophysical Union.

Korenaga, J. (2007a). Effective thermal expansivity of Maxwellian oceanic lithosphere. *Earth Planet. Sci. Lett.*, *257*, 343-349.

Korenaga, J. (2007b). Eustasy, supercontinental insulation, and the temporal variability of terrestrial heat flux. *Earth Planet. Sci. Lett.*, *257*, 350-358.

Korenaga, J. (2007c). Thermal cracking and the deep hydration of oceanic lithosphere: A key to the generation of plate tectonics? *J. Geophys. Res.*, *112*, B05408, doi:10.1029/2006JB004502.

Korenaga, J. (2008). Urey ratio and the structure and evolution of Earth's mantle. *Rev. Geophys.*, *46*, RG2007, doi:10.1029/2007RG000241.

Korenaga, J. (2009). How does small-scale convection manifest in surface heat flux? *Earth Planet. Sci. Lett.*, *287*, 329-322.

Korenaga, J. (2015). Seafloor topography and the thermal budget of Earth. In G. R. Foulger, M. Lustrino, & S. D. King (Eds.), *The Interdisciplinary Earth: A Volume in Honor of Don L. Anderson* (p. 167-185). Geological Society of America.

Korenaga, J. (2017a). On the extent of mantle hydration by plate bending. *Earth Planet. Sci. Lett.*, *457*, 1-9.

Korenaga, J. (2017b). Pitfalls in modeling mantle convection with internal heating. *J. Geophys. Res. Solid Earth*, *122*, 4064-4085, doi:10.1002/2016JB013850.

Korenaga, J. (2018). Crustal evolution and mantle dynamics through Earth history. *Phil. Trans. R. Soc. A*, *376*, 20170408, http://dx.doi.org/10.1098/rsta.2017.0408.

Korenaga, J. (2020). Plate tectonics and surface environment: Role of the oceanic upper mantle. *Earth-Sci. Rev.*, *205*, 103185, https://doi.org/10.1016/j.earscirev.2020.103185.

Korenaga, J., Holbrook, W. S., Detrick, R. S., & Kelemen, P. B. (2001). Gravity anomalies and crustal structure at the Southeast Greenland margin. *J. Geophys. Res.*, *106*, 8853-8870.

Korenaga, J., & Jordan, T. H. (2003). Physics of multiscale convection in Earth's mantle: Onset of sublithospheric convection. *J. Geophys. Res.*, *108*(B7), 2333, doi:10.1029/2002JB001760.

Korenaga, J., & Jordan, T. H. (2004). Physics of multiscale convection in Earth's mantle: Evolution of sublithospheric convection. *J. Geophys. Res.*, *109*, B01405, doi:10.1029/2003JB002464.

Korenaga, J., Kelemen, P. B., & Holbrook, W. S. (2002). Methods for resolving the origin of large igneous provinces from crustal seismology. *J. Geophys. Res.*, *107*(B9), 2178, doi:10.1029/2001JB001030.

Korenaga, J., Planavsky, N. J., & Evans, D. A. D. (2017). Global water cycle and the coevolution of Earth's interior and surface environment. *Phil. Trans. R. Soc. A*, *375*, 20150393, doi:10.1098/rsta.2015.0393.

Korenaga, T., & Korenaga, J. (2008). Subsidence of normal oceanic lithosphere, apparent thermal expansivity, and seafloor flattening. *Earth Planet. Sci. Lett.*, *268*, 41-51.

Korenaga, T., & Korenaga, J. (2016). Evolution of young oceanic lithosphere and the meaning of seafloor subsidence rate. *J. Geophys. Res. Solid Earth*, *121*, 6315-6332, doi:10.1002/2016JB013395.

Langseth, M. G., Le Pichon, X., & Ewing, M. (1966). Crustal structure of the mid-ocean ridges, 5, heat flow through the Atlantic ocean floor and convection currents. *J. Geophys. Res.*, *71*, 5321-5355.

Lister, C. R. B. (1977). Estimators for heat flow and deep rock properties based on boundary layer theory. *Tectonophysics*, *41*, 157-171.

Lister, C. R. B., Sclater, J. G., Davis, E. E., Villinger, H., & Nagihara, S. (1990). Heat flow maintained in ocean basins of great age: investigations in the north-equatorial west Pacific. *Geophys. J. Int.*, *102*, 603-628.

Lowman, J. P., King, S. D., & Gable, C. W. (2003). The role of the heating mode of the mantle in intermittent reorganization of the plate velocity field. *Geophys. J. Int.*, *152*, 455-467.

Lyubetskaya, T., & Korenaga, J. (2007a). Chemical composition of Earth's primitive mantle and its variance, 1, methods and results. *J. Geophys. Res.*, *112*, B03211, doi:10.1029/2005JB004223.

Lyubetskaya, T., & Korenaga, J. (2007b). Chemical composition of Earth's primitive man-

tle and its variance, 2, implications for global geodynamics. *J. Geophys. Res.*, *112*, B03212, doi:10.1029/2005JB004224.

Maggi, A., Debayle, E., Priestley, K., & Barruol, G. (2006). Multimode surface waveform tomography of the Pacific Ocean: a closer look at the lithospheric cooling signature. *Geophys. J. Int.*, *166*, 1384-1397.

Marty, J. C., & Cazenave, A. (1989). Regional variations in subsidence rate of oceanic plates: a global analysis. *Earth Planet. Sci. Lett.*, *94*, 301-315.

McDonough, W. F., & Sun, S.-s. (1995). The composition of the Earth. *Chem. Geol.*, *120*, 223-253.

McKenzie, D. (1978). Some remarks on the development of sedimentary basins. *Earth Planet. Sci. Lett.*, *40*, 25-32.

McKenzie, D., Jackson, J., & Priestley, K. (2005). Thermal structure of oceanic and continental lithosphere. *Earth Planet. Sci. Lett.*, *233*, 337-349.

McKenzie, D. P. (1967). Some remarks on heat flow and gravity anomalies. *J. Geophys. Res.*, *72*, 6261-6273.

McNutt, M. K. (1984). Lithospheric flexure and thermal anomalies. *J. Geophys. Res.*, *89*, 11180-11194.

Mehouachi, F., & Singh, S. C. (2018). Water-rich sublithospheric melt channel in the equatorial Atlantic Ocean. *Nature Geosci.*, *11*, 65-69.

Minshull, T. A. (2009). Geophysical characterisation of the ocean–continent transition at magma-poor rifted margins. *C. R. Geoscience*, *341*, 382-393.

Mishra, J. K., & Gordon, R. G. (2016). The rigid-plate and shrinking-plate hypothesis: Implications for the azimuths of transform faults. *Tectonics*, *35*, 1827-1842, doi:10.1002/2015TC003968.

Morishige, M., Honda, S., & Yoshida, M. (2010). Possibility of hot anomaly in the sub-slab mantle as an origin of how seismic velocity anomaly under the subducting Pacific plate. *Phys. Earth Planet. Inter.*, *183*, 353-365.

Nagihara, S., Lister, C. R. B., & Sclater, J. G. (1996). Reheating of old oceanic lithosphere: Deductions from observations. *Earth Planet. Sci. Lett.*, *139*, 91-104.

Parsons, B. (1982). Causes and consequences of the relation between area and age of the ocean floor. *J. Geophys. Res.*, *87*, 289-302.

Parsons, B., & Daly, S. (1983). The relationship between surface topography, gravity anomalies, and temperature structure of convection. *J. Geophys. Res.*, *88*, 1129-1144.

Parsons, B., & McKenzie, D. (1978). Mantle convection and the thermal structure of the plates. *J. Geophys. Res.*, *83*, 4485-4496.

Parsons, B., & Sclater, J. G. (1977). An analysis of the variation of ocean floor bathymetry and heat flow with age. *J. Geophys. Res.*, *82*(5), 803-827.

Pollack, H. N. (1980). On the use of the volumetric thermal expansion coefficient in models of ocean floor topography. *Tectonophysics*, *64*, T45-T47.

Priestley, K., & McKenzie, D. (2013). The relationship between shear wave velocity, temperature, attenuation and viscosity in the shallow part of the mantle. *Earth Planet. Sci. Lett.*, *381*, 78-91.

Richards, F., Hoggard, M., Crosby, A., Ghelichkhan, S., & White, N. (2020). Structure and dynamics of the oceanic lithosphere-asthenosphere system. *Phys. Earth Planet. Inter.*, *309*, 106559.

Richards, F. D., Hoggard, M. J., Cowton, L. R., & White, N. J. (2018). Reassessing the thermal structure of oceanic lithosphere with revised global inventories of basement depths and heat flow measurements. *J. Geophys. Res. Solid Earth*, *123*, 9136-9161, https://doi.org/10.1029/2018JB015998.

Richardson, W. P., Stein, S., Stein, C. A., & Zuber, M. T. (1995). Geoid data and thermal structure of the oceanic lithosphere. *Geophys. Res. Lett.*, *22*, 1913-1916.

Ritzwoller, M. H., Shapiro, N. M., & Zhong, S. (2004). Cooling history of the Pacific lithosphere. *Earth Planet. Sci. Lett.*, *226*, 69-84.

Rosas, J. C., & Korenaga, J. (2021). Archean seafloor shallowed with age due to radiogenic heating in the mantle. *Nature Geosci.*, *14*, 51-56, https://doi.org/10.1038/s41561-020-00673-1.

Rudnick, R. L., & Gao, S. (2003). Composition of the continental crust. In H. D. Holland & K. K. Turekian (Eds.), *Treatise on Geochemistry* (Vol. 3, p. 1-64). Elsevier.

Salters, V. J. M., & Stracke, A. (2004). Composition of the depleted mantle. *Geochem. Geophys. Geosys.*, *5*, Q05004, doi:10.1029/2003GC000597.

Sarafian, E., Evans, R. L., Collins, J. A., Elsenbeck, J., Gaetani, G. A., Gaherty, J. B., ... Lizarralde, D. (2015). The electrical structure of the central Pacific upper mantle constrained by the NoMelt experiment. *Geochem. Geophys. Geosys.*, *16*, 1115-1132, doi:10.1002/2014GC005709.

Schaeffer, A. J., & Lebedev, S. (2013). Global shear speed structure of the upper mantle and transition zone. *Geophys. J. Int.*, *194*, 417-449.

Schroeder, W. (1984). The empirical age-depth relation and depth anomalies in the Pacific ocean basin. *J. Geophys. Res.*, *89*, 9873-9883.

Schubert, G., & Reymer, A. P. S. (1985). Continental volume and freeboard through geological time. *Nature*, *316*, 336-339.

Seton, M., Müller, R. D., Zahirovic, S., Williams, S., Wright, N. W., Cannon, J., ... McGirr, R. (2020). A global data set of present-day oceanic crustal age and seafloor spreading parameters. *Geochem. Geophys. Geosys.*, *21*, e2020GC009214, https://doi.org/10.1029/2020GC009214.

Smith, W. H. F., & Sandwell, D. T. (1997). Global sea floor topography from satellite altimetry and ship depth soundings. *Science*, *277*, 1956-1962.

Sobolev, A. V., Hofmann, A. W., Kuzmin, D. V., Yaxley, G. M., Arndt, N. T., Chung, S.-L., ... Teklay, M. (2007). The amount of recycled crust in sources of mantle-derived melts. *Science*, *316*, 412-417.

Solomatov, V. S., & Barr, A. C. (2007). Onset of convection in fluids with strongly temperature-dependent, power-law viscosity, 2. dependence on the initial perturbation. *Phys. Earth Planet. Inter.*, *165*, 1-13.

Solomatov, V. S., & Moresi, L.-N. (2000). Scaling of time-dependent stagnant lid convection: Application to small-scale convection on Earths and other terrestrial planets. *J. Geophys. Res.*, *105*, 21795-21817.

Stein, C. A., & Stein, S. (1992). A model for the global variation in oceanic depth and heat flow with lithospheric age. *Nature*, *359*, 123-129.

Stixrude, L., & Lithgow-Bertelloni, C. (2005). Thermodynamics of mantle minerals, I, physical properties. *Geophys. J. Int.*, *162*, 610-632.

Straume, E. O., Gaina, C., Medvedev, S., Hochmuth, K., Gohl, K., Whittaker, J. M., ... Hopper, J. R. (2019). GlobSed: Updated total sediment thickness in the world's oceans. *Geochem. Geophys. Geosys.*, *20*, 1756-1772.

Syracuse, E. M., van Keken, P. E., & Abers, G. A. (2010). The global range of subduction zone thermal models. *Phys. Earth Planet. Inter.*, *183*, 73-90.

Takeo, A., Kawakatsu, H., Isse, T., Nishida, K., Shiobara, H., Sugioka, H., ... Utada, H. (2018). Is situ characterization of the lithosphere-asthenosphere system beneath NW Pacific Ocean broadband dispersion survey with two OBS arrays. *Geochem. Geophys. Geosys.*, *19*, https://doi.org/10.1029/2018GC007588.

Tolstoy, M., Harding, A. J., & Orcutt, J. A. (1993). Crustal thickness on the Mid-Atlantic Ridge: bull's eye gravity anomalies and focused accretion. *Science*, *262*, 726-729.

Turcotte, D. L. (1974). Are transform faults thermal contraction cracks? *J. Geophys. Res.*, *79*, 2573-2577.

Turcotte, D. L., & Oxburgh, E. R. (1973). Mid-plate tectonics. *Nature*, *244*, 337-339.

Van Avendonk, H. J. A., Davis, J. K., Harding, J. L., & Lawver, L. A. (2017). Decrease in oceanic crustal thickness since the breakup of Pangaea. *Nature Geosci.*, *10*, 58-61.

Van Avendonk, H. J. A., Holbrook, W. S., Nunes, G. T., Shillington, D. J., Tucholke, B. E., Louden, K. E., ... Hopper, J. R. (2006). Seismic velocity structure of the rifted margin of the eastern Grand Banks of Newfoundland, Canada. *J. Geophys. Res.*, *111*, B11404, doi:10.1029/2005JB004156.

Von Herzen, R. P. (2004). Geothermal evidence for continuing hydrothermal circulation in older (>60 M.y.) ocean crust. In E. E. Davis & H. Elderfield (Eds.), *Hydrogeology of*

the oceanic lithosphere. Cambridge Univ. Press.

Von Herzen, R. P., & Uyeda, S. (1963). Heat flow through the eastern pacific ocean floor. *J. Geophys. Res.*, *68*, 4219-4250.

Watts, A. B., Bodine, J. H., & Ribe, N. M. (1980). Observations of flexure and the geological evolution of the Pacific Ocean Basin. *Nature*, *283*, 532-537.

White, R., & McKenzie, D. (1989). Magmatism at rift zones: The generation of volcanic continental margins and flood basalts. *J. Geophys. Res.*, *94*, 7685-7729.

White, R. S., Smith, L. K., Roberts, A. W., Christie, P. A. F., Kusznir, N. J., & iSIMM Team. (2008). Lower-crustal intrusion on the North Atlantic continental margin. *Nature*, *452*, 460-464.

Wolf, A. S., Jackson, J. M., Dera, P., & Prakapenka, V. B. (2015). The thermal equation of state of (Mg, Fe)SiO_3 bridgmanite (perovskite) and implications for lower mantle structures. *J. Geophys. Res. Solid Earth*, *120*, 7460-7489, doi:10.1002/2015JB012108.

Workman, R. K., & Hart, S. R. (2005). Major and trace element composition of the depleted MORB mantle (DMM). *Earth Planet. Sci. Lett.*, *231*, 53-72.

Yamamoto, J., Korenaga, J., Nirano, N., & Kagi, H. (2014). Melt-rich lithosphere-asthenosphere boundary inferred from petit-spot volcanoes. *Geology*, *42*, 967-970.

Yamano, M., Hamamoto, H., Kawada, Y., & Goto, S. (2014). Heat flow anomaly on the seaward side of the Japan Trench associated with deformation of the incoming Pacific plate. *Earth Planet. Sci. Lett.*, *407*, 196-204.

Yamauchi, H., & Takei, Y. (2016). Polycrystal anelasticity at nearsolidus temperatures. *J. Geophys. Res. Solid Earth*, *121*, 7790– 7820, https://doi.org/10.1002/2016JB013316.

Yuan, X., Korenaga, J., Holbrook, W. S., & Kelemen, P. B. (2020). Crustal structure of the Greenland-Iceland Ridge from joint refraction and reflection seismic tomography. *J. Geophys. Res. Solid Earth*, *125*, e2020JB019847, https://doi.org/10.1029/2020JB019847.

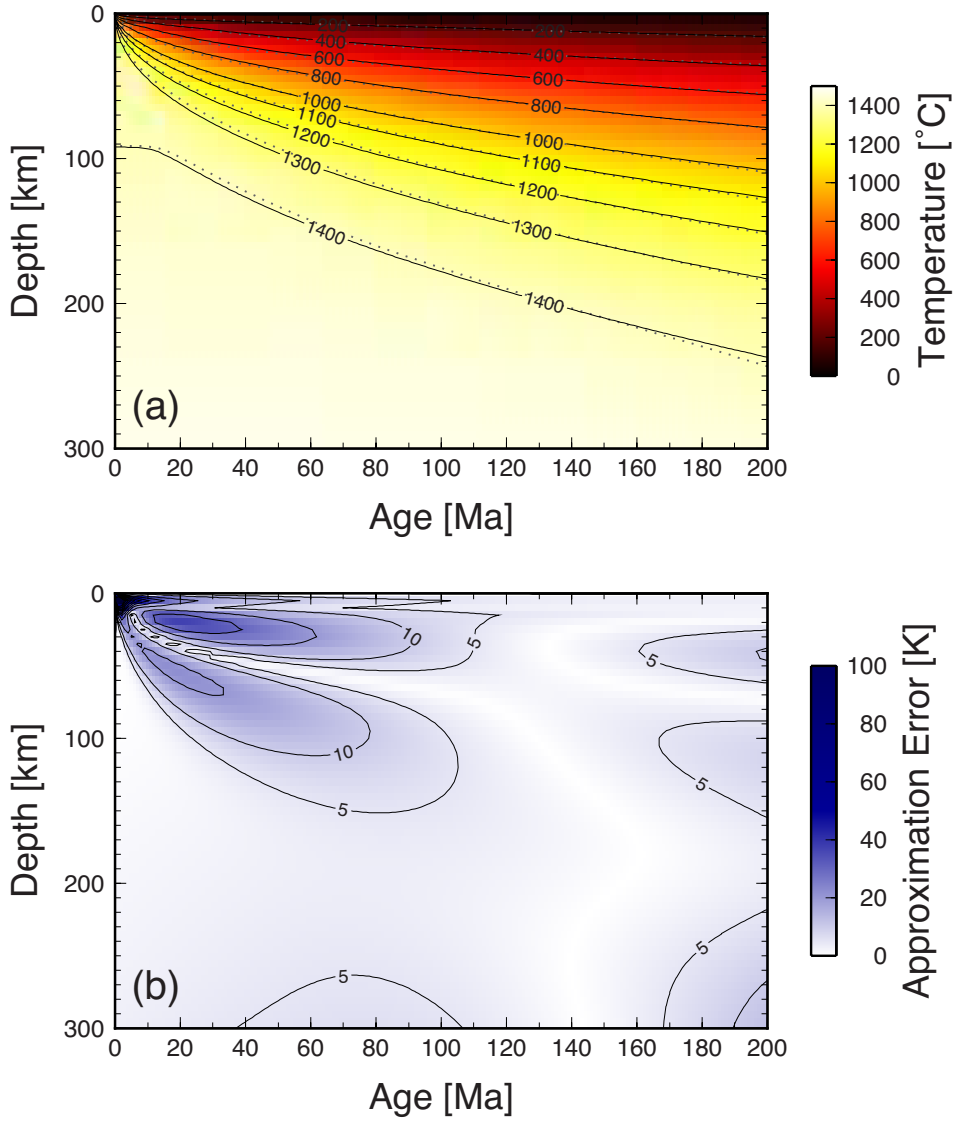

Figure 1. (a) Thermal evolution of the suboceanic mantle according to the thermal conduction modeling of Korenaga and Korenaga (2016). Isotherms for our parameterization of the numerical model (equation (2)) are shown in dotted. (b) Absolute approximation error of our parameterization.

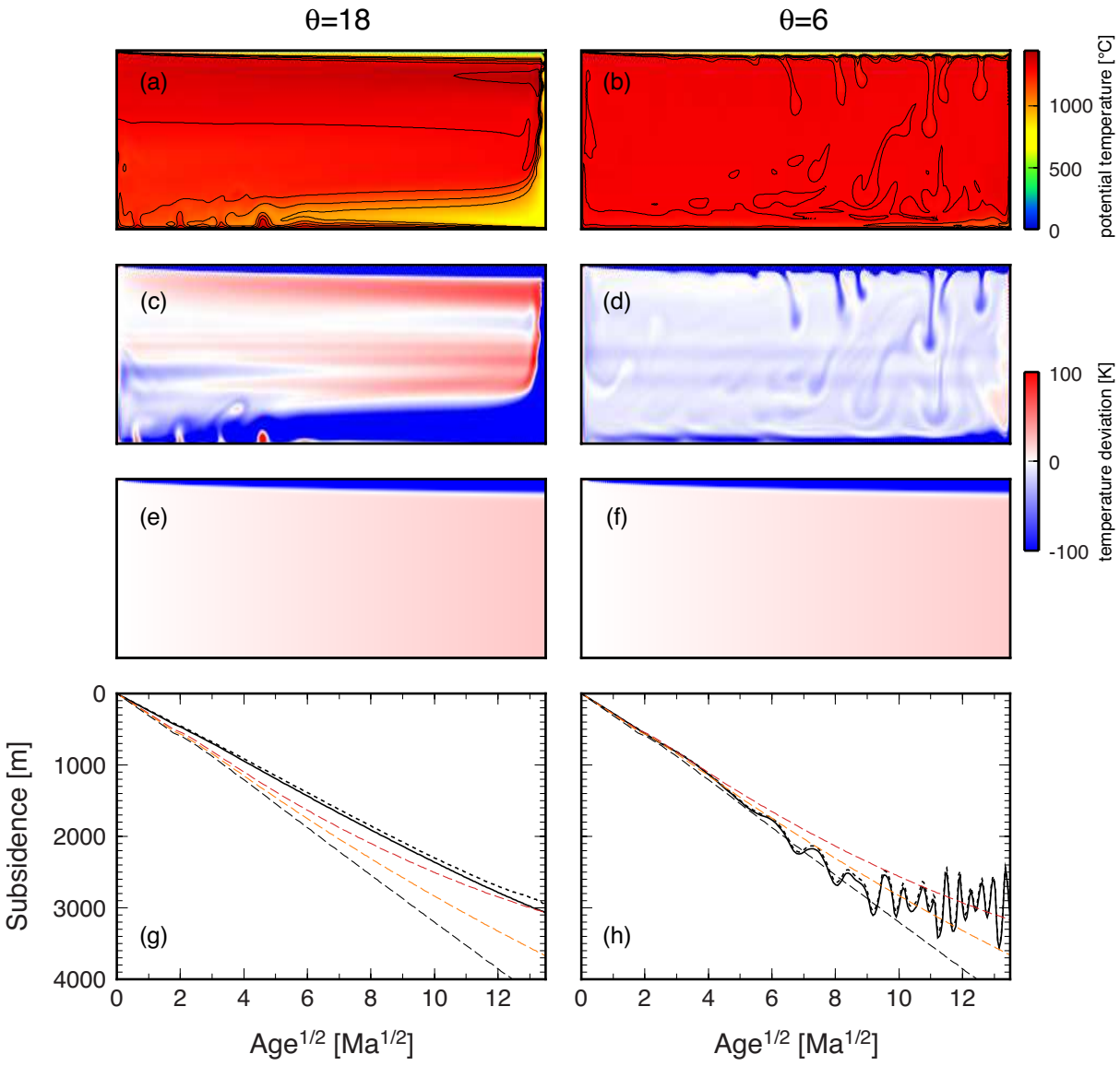

Figure 2. Examples of convection modeling in a closed domain (See Supporting Information for the details of numerical modeling). The left and right columns correspond to the cases with the Frank-Kamenetskii parameter, θ, of 18 and 6, respectively. The aspect ratio of the model domain is 4:1, so the lateral extent corresponds to 11600 km. In both cases, the Rayleigh number of 10^9 is used, internal heat production is set at $\sim 1.6 \times 10^{-12}$ W kg^{-1}, and the surface plate is moved with a velocity of 5.43 cm yr^{-1}. (a) Snapshot of the temperature field for the case of θ=18 at a model time of $\sim$3.66 Ga. Isothermal contours are drawn for 1000 to 1400 °C at an interval of 100 K. The system is cooling down at the rate of $\sim$50 K Ga^{-1} (Figure S1). (b) Snapshot for the case of θ=6 at a model time of $\sim$1.85 Ga. The system is cooling down at the rate of $\sim$40 K Ga^{-1}. Subduction flow is barely visible because its thickness is limited. (c) and (d) are same as (a) and (b), respectively, but expressed as difference from the column beneath the ridge axis (the left side). (e) and (f) are temperature variations with respect to the mantle column beneath the ridge axis, corresponding to our reference model (with an internal heating of $\sim 1.6 \times 10^{-12}$ W kg^{-1} and a secular cooing rate of 50 K Ga^{-1} and 40 K Ga^{-1}, respectively). (g) and (h) are corresponding subsidence curves, based on convection snapshots shown in (a) and (b) (thick solid), only the upper half of the snapshots (thick dotted), pure half-space cooling (no internal heating and secular cooling) (dashed), half-space cooling with internal heating (orange dashed), and half-space cooling with internal heating and secular cooling (red dashed).

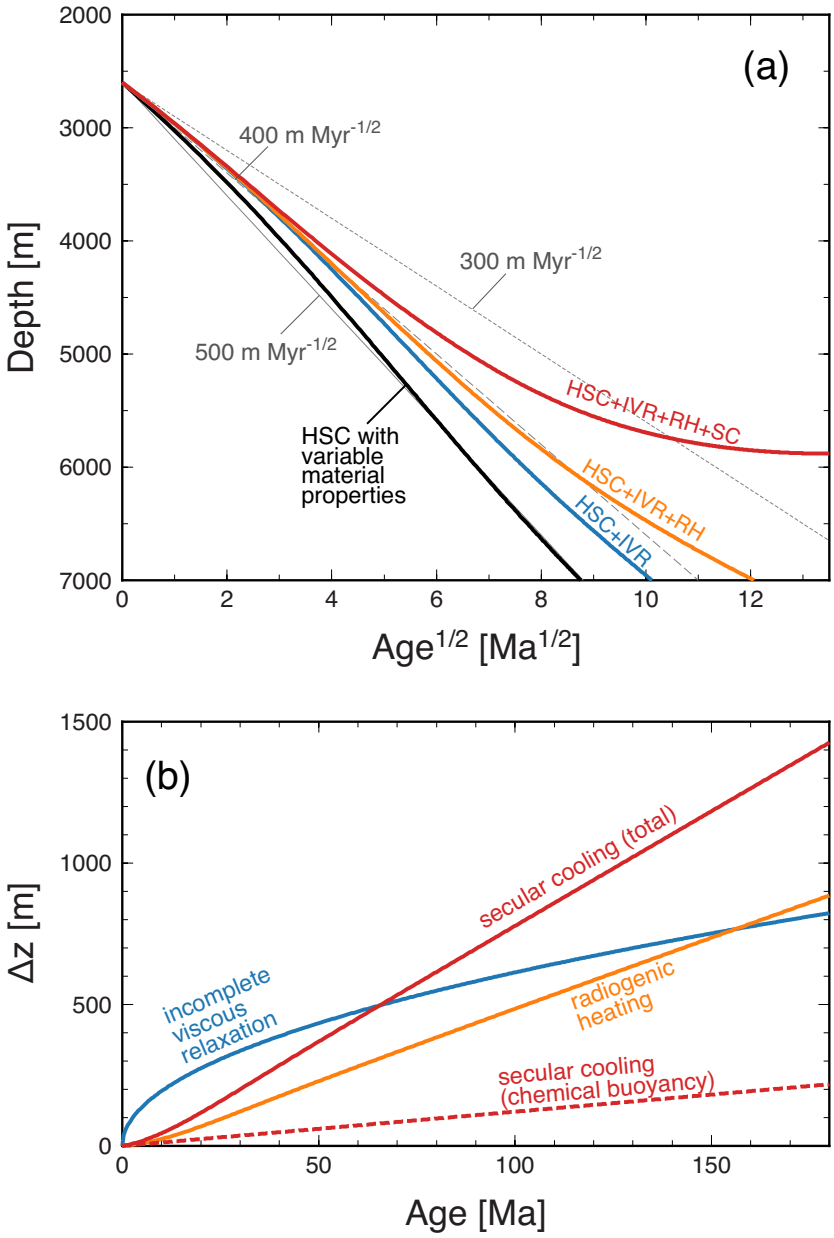

Figure 3. (a) Predicted age-depth relationship according to equation (14) for the reference case: the radiogenic heating of 2.3×10^{-12} W kg^{-1}, the secular cooling rate of 100 K Ga^{-1}, the viscosity contrast between the upper and lower mantle of 10, the topography scale of 1.7×10^5 m, whole-mantle thermal anomaly, the plate length of 11600 km, and f_{TC}=0.85. Subsidence with half-space cooling (HSC) with variable material properties is shown in black, with the cumulative effects of adding incomplete viscous relaxation (HSC+IVR; blue), radiogenic heating (HSC+IVR+RH; orange), and secular cooling (HSC+IVR+RH+SC; red). Also shown in gray are cases with constant subsidence rates (300-500 m Ma$^{-1/2}$). (b) Effects of incomplete viscous relaxation (blue), radiogenic heating (orange), and secular cooling (red) are shown as a function of age, for the reference case shown in (a). The effect of varying chemical buoyancy associated secular cooling is shown in dashed red line.

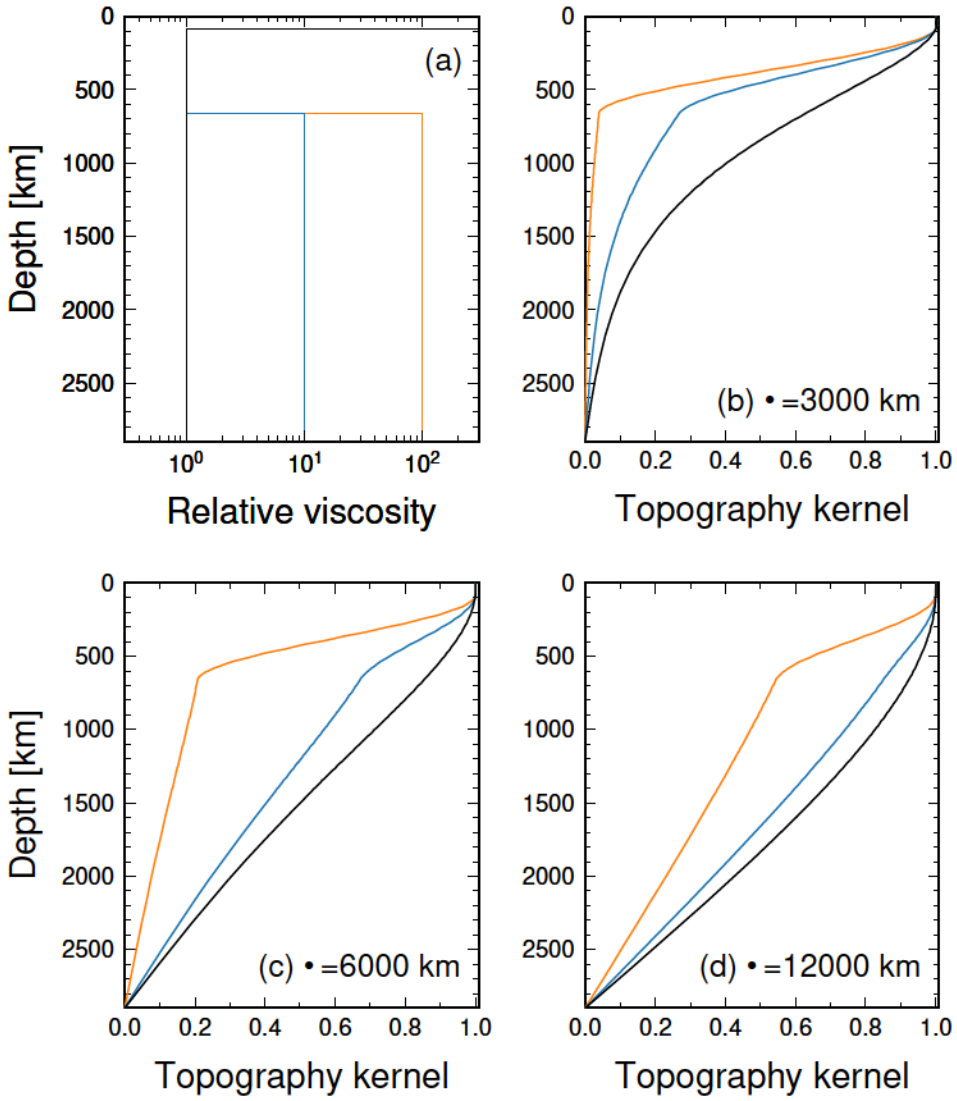

Figure 4. (a) Three viscosity profiles used for the calculation of topography kernels shown in (b)-(d). All profiles have a 100-km thick lithosphere, which has a relative viscosity of 10^4. The lower mantle has a relative viscosity of 1 (black), 10 (blue), and 100 (orange). Corresponding topography kernels, calculated with the propagator matrix method (Hager & O'Connell, 1981), are shown for wavelengths of (b) 3000 km, (c) 6000 km, and (d) 12000 km. Note that the concept of topography kernel is valid only when viscosity variations are limited to the vertical direction. The calculation of surface topography in this study is done with viscosities varying both horizontally and vertically, and topography kernels are computed here solely for discussion.

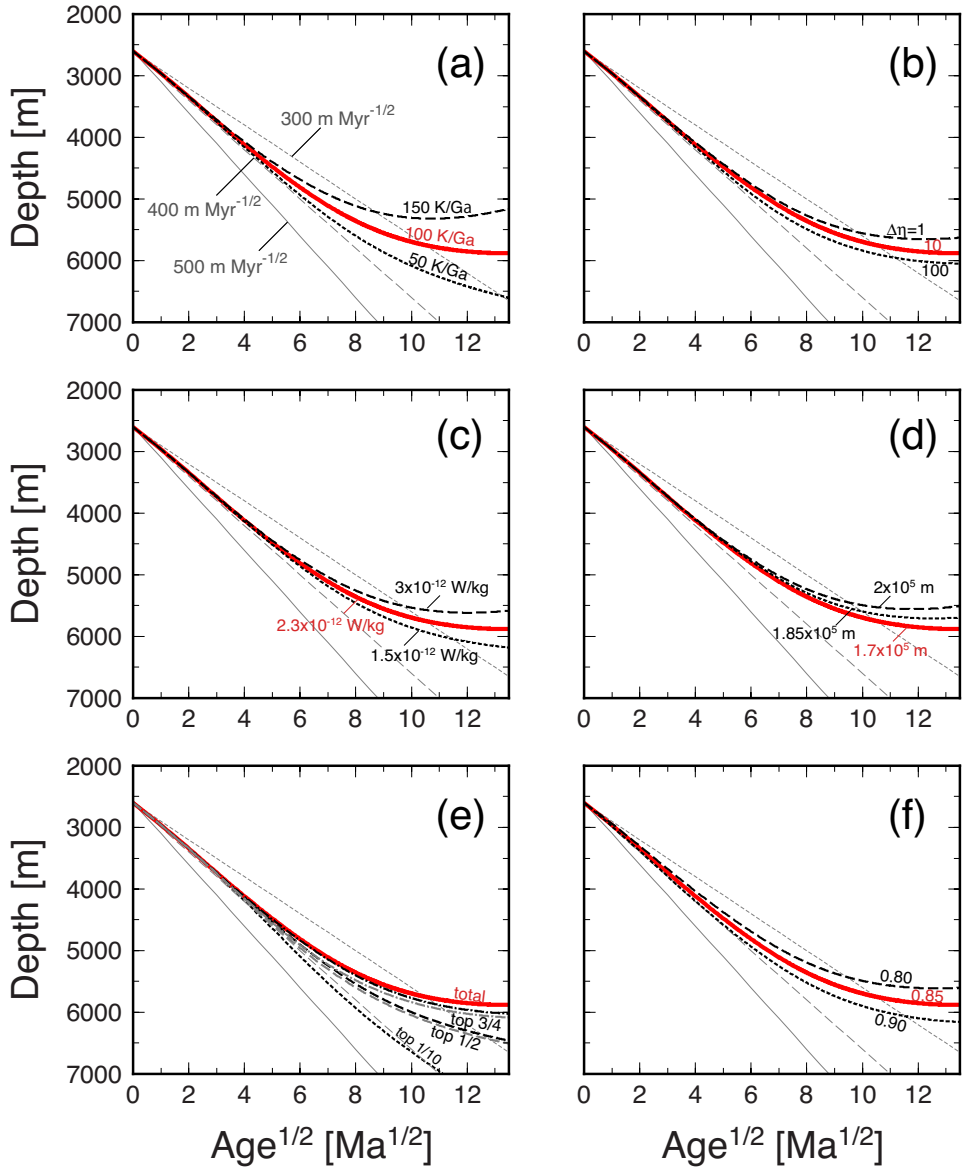

Figure 5. Sensitivty of predicted subsidence with respect to the reference case (shown in red in all panels). As in Figure 3, cases with constant subsidence rates (300-500 m Ma$^{-1/2}$) are also shown in gray. (a) Effect of varying secular cooling: 50 K Gyr^{-1} (dotted) and 150 K Gyr^{-1} (dashed). (b) Effect of varying viscosity contrast between the upper and lower mantle: 1 (dotted) and 100 (dashed). (c) Effect of varying radiogenic heating: 1.5×10^{-12} W kg^{-1} (dotted) and 3×10^{-12} W kg^{-1} (dashed). (d) Effect of varying topographic scale: 1.85×10^5 m (dotted) and 2×10^5 m (dashed). (e) Effect of varying the depth extent of thermal anomalies (caused by both radiogenic heating and secular cooling) as well as plate length: top 3/4 (dot-dashed), top 1/2 (dashed), and top 1/10 (dotted). For the case of no thermal anomalies at all from radiogenic heating and secular cooling, see the HSC+IVR curve in Figure 3a. Shown in gray are cases with the plate length of 5800 km (difference in plate length does not cause a discernable change for the top 1/10 case). (f) Effect of varying the extent of incomplete viscous relaxation: f_{TC} of 0.8 (dotted) and 0.9 (dashed).

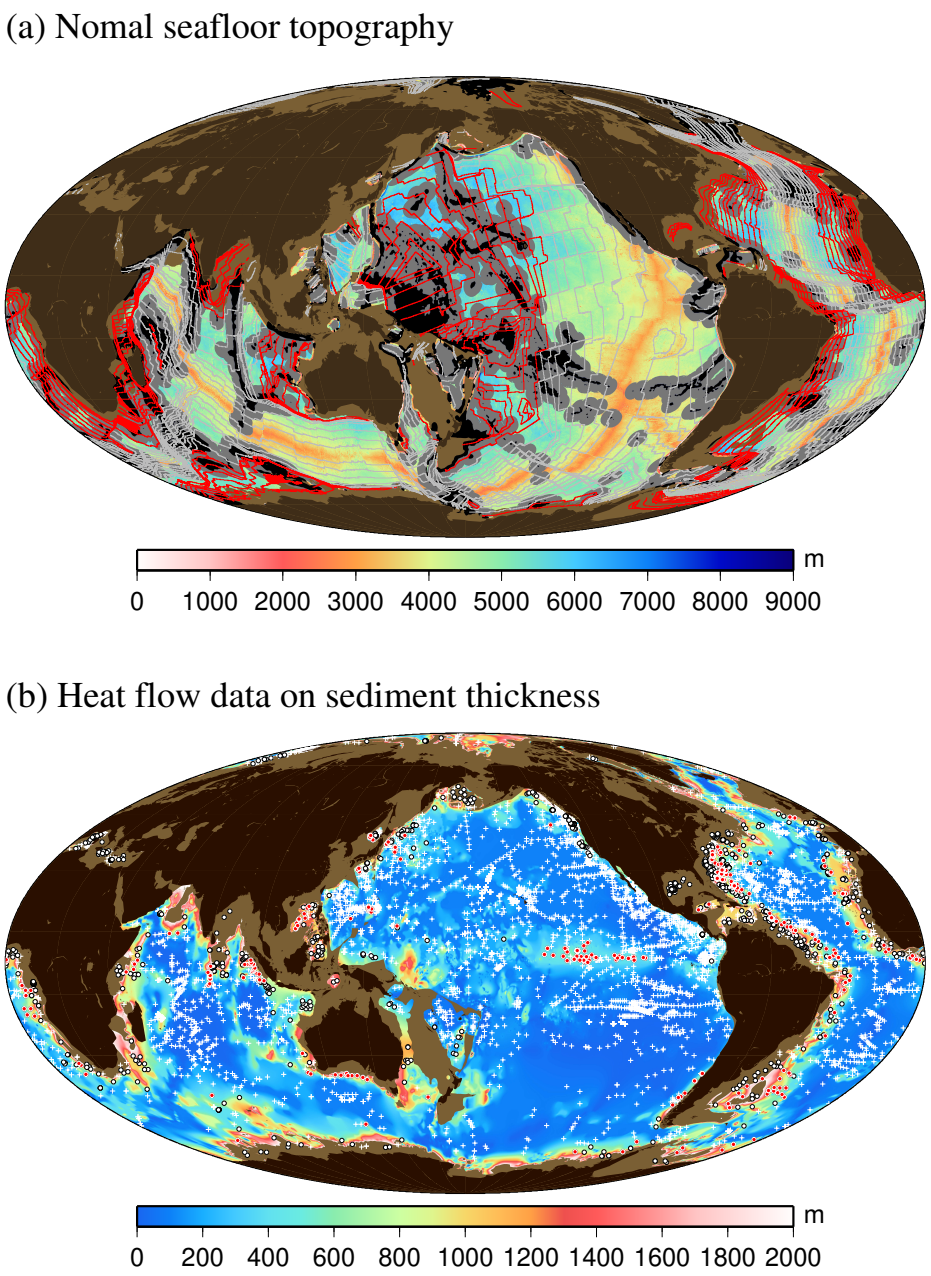

Figure 6. (a) Seafloor topography according the ETOPO1 model (Amante & Eakins, 2009), with isochrons for seafloor age (Seton et al., 2020) (red contours for ages greater than 80 Ma ago). Black shading denotes 'anomalous crust' regions with residual depths (with respect to the reference model of Stein and Stein (1992)) greater than 1 km, which corresponds to the hotspot chains and oceanic plateaus. Gray shading denotes the regions of 300 km distance to the nearest anomalous crust. Light brown denotes where either age or sediment data are unavailable, or sediments are thicker than 2 km. The part of seafloor not covered by any of these shadings corresponds to the 'normal seafloor' used in this work. (b) The spatial distribution of marine heat flow data, plotted on sediment thickness of Straume et al. (2019). White crosses denote available heat flow data after prescreening, white circles denote data filtered with the minimum distance of 60 km from nearby seamounts and the minimum sediment thickness of 400 m (see text for details), and red circles denote the same filtered data but on the normal seafloor as defined in (a).

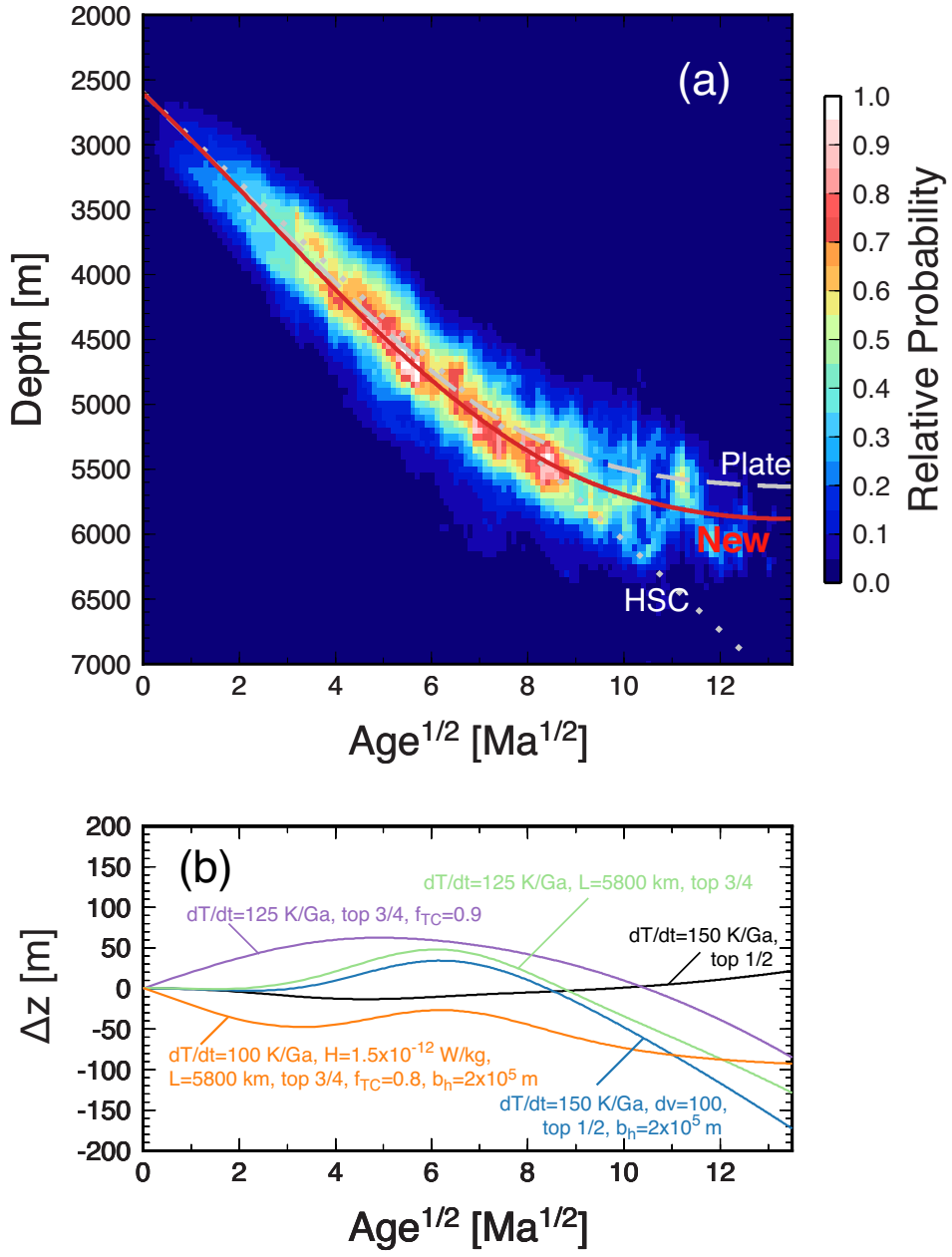

Figure 7. (a) The age-depth relation for the normal seafloor, with the new reference model (equation 14; red), the half-space cooling model of Carlson and Johnson (1994) (dotted), and the plate model of Stein and Stein (1992) (dashed). (b) Examples of other combinations of model parameters that yield similar subsidence behaviors to the reference case. Difference from the reference case is shown as a function of age$^{1/2}$; negative difference indicates shallower seafloor with respect to the reference case. Labels denote parameters different from the reference case, which is specified by the radiogenic heating of 2.3×10^{-12} W kg^{-1}, the secular cooling rate of 100 K Ga^{-1}, the viscosity contrast between the upper and lower mantle of 10, the topography scale of 1.7×10^5 m, whole-mantle thermal anomaly, the plate length of 11600 km, and f_{TC}=0.85.

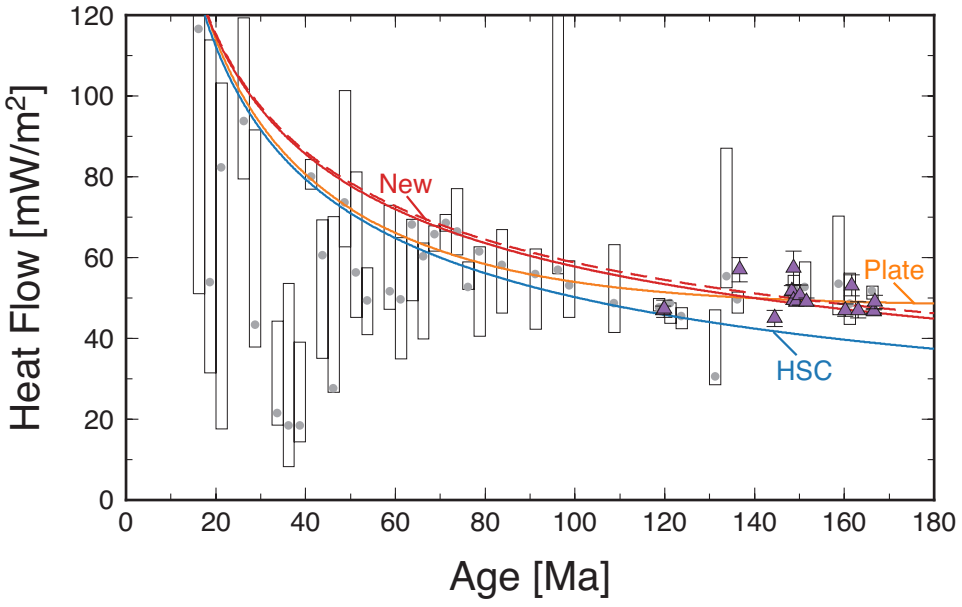

Figure 8. The age-heat flow relationship of normal seafloor. The width of age bin is 2.5 Ma, and age bins with more than four data points are shown. Boxes extend from the first to the third quartile of data in each bin, and gray circles denote median. High-quality heat flow data on old seafloor compiled by Lister et al. (1990) and Nagihara et al. (1996), which are included in the compilation of Hasterok (2010), are highlighted as purple triangles; we only show their data on normal seafloor. Also shown are the new reference model: equation (4) (red) and equation (16) (red dashed), with the half-space cooling model of Lister (1977) (blue) and the plate model of Stein and Stein (1992) (orange).

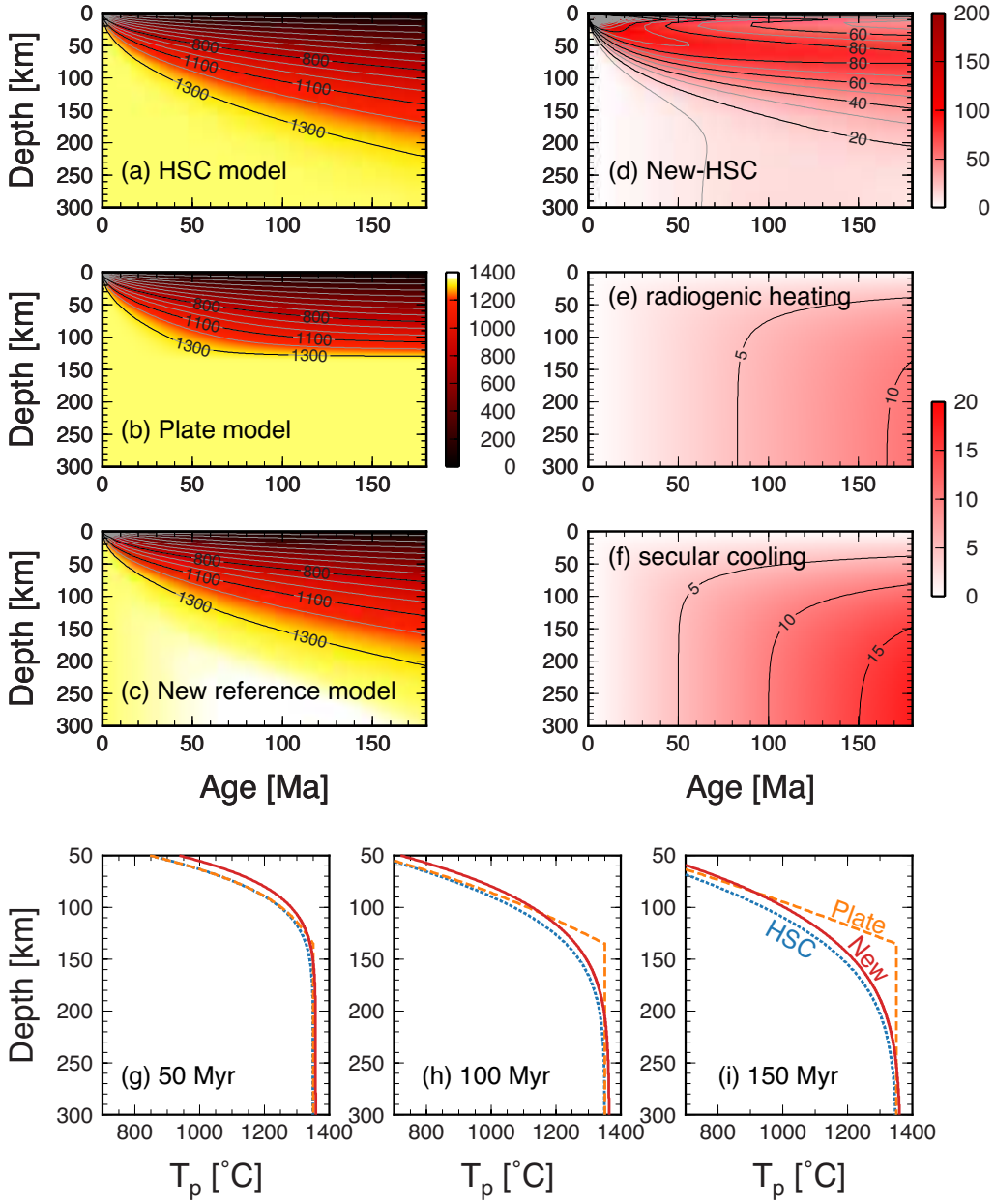

Figure 9. Comparison of (a) the traditional half-space cooling model with κ of 10^{-6} m^2 s^{-1}, (b) the plate model with a plate thickness of 135 km, and (c) the new reference model. Potential temperature is used here for simplicity.; i.e., $a_1 z + a_2 z^2$ in equation (2) is neglected for the new reference model. (d) Difference between the new reference model and the traditional half-space cooling model. (e) Radiogenic heating component and (f) secular cooling component in equation (7). Geotherms of these reference models are compared at (g) 50 Ma, (h) 100 Ma, and (i) 150 Ma: the new reference model (equation 17; red), the traditional HSC model (blue), and the plate model (orange).

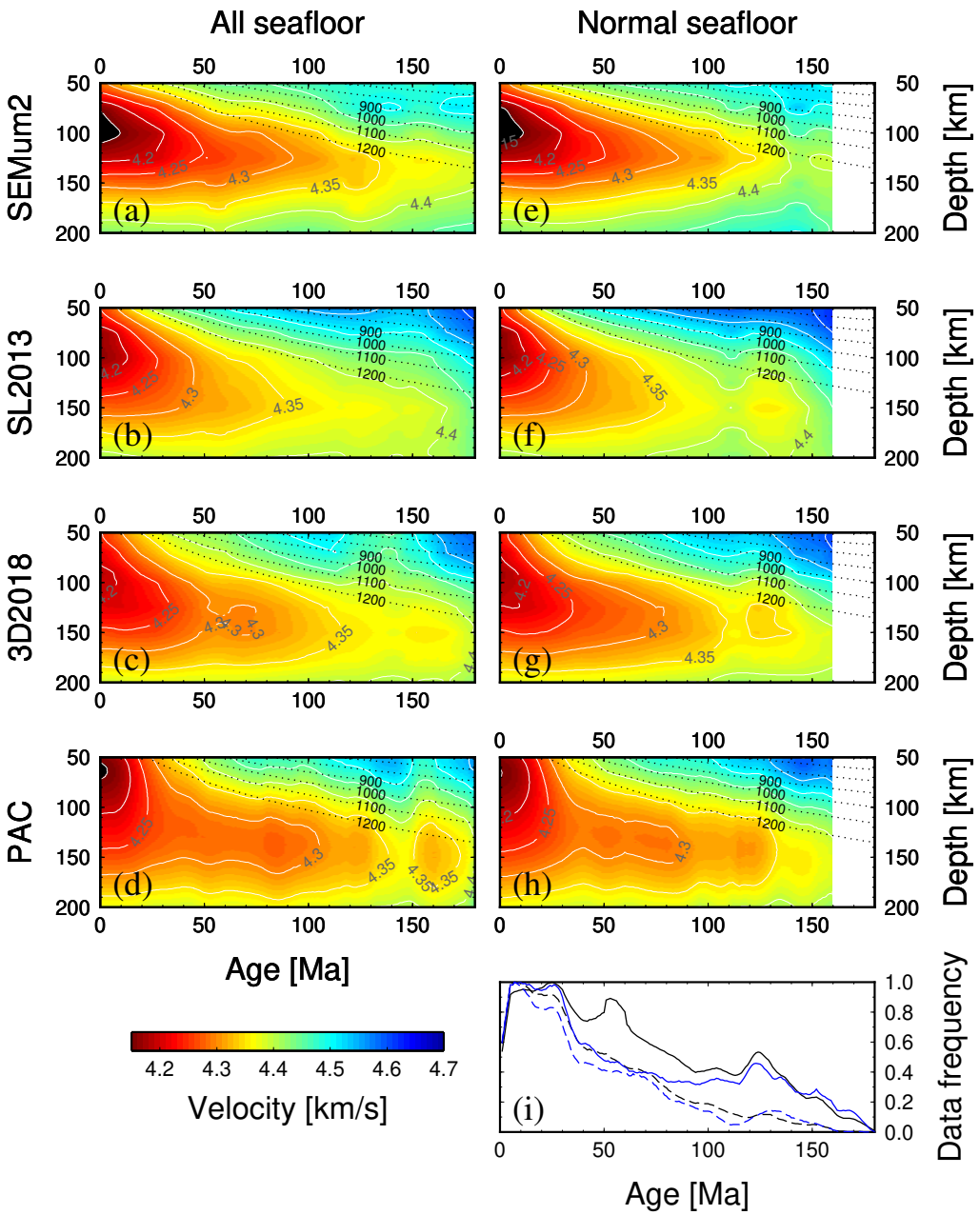

Figure 10. Age-stacked β_V models calculated from four different surface tomography models: (a,e) SEMum2 (French et al., 2013), (b,f) SL2013 (Schaeffer & Lebedev, 2013), (c,g) 3D2018 (Debayle et al., 2016), and (d,h) PAC-age (Isse et al., 2019). To focus on the evolution of oceanic lithosphere, the depth range of 50 to 200 km is shown. Age stacking is done with 5 Ma bin, under (left) all seafloor and (right) normal seafloor. As these models are constructed with different reference periods (1 s for SEMum2 and PAC-age, 50 s for SL2013, and 100 s for 3D2018), they are compared at a reference period of 50 s, by taking into account the effect of physical dispersion with Q_S of 100. For normal seafloor, stacking for ages greater than 160 Ma ago is not possible because of lack of data. Dotted lines in (a)-(h) are isothermal contours based on the new reference model (equation (17)); they represent actual temperatures, not potential temperatures. Model PAC-age covers only the Pacific upper mantle, whereas other models are global. Data frequency per age bin is shown in (i): black line for (a)-(c), black dashed line for (e)-(g), blue line for (d), blue dashed line for (h).

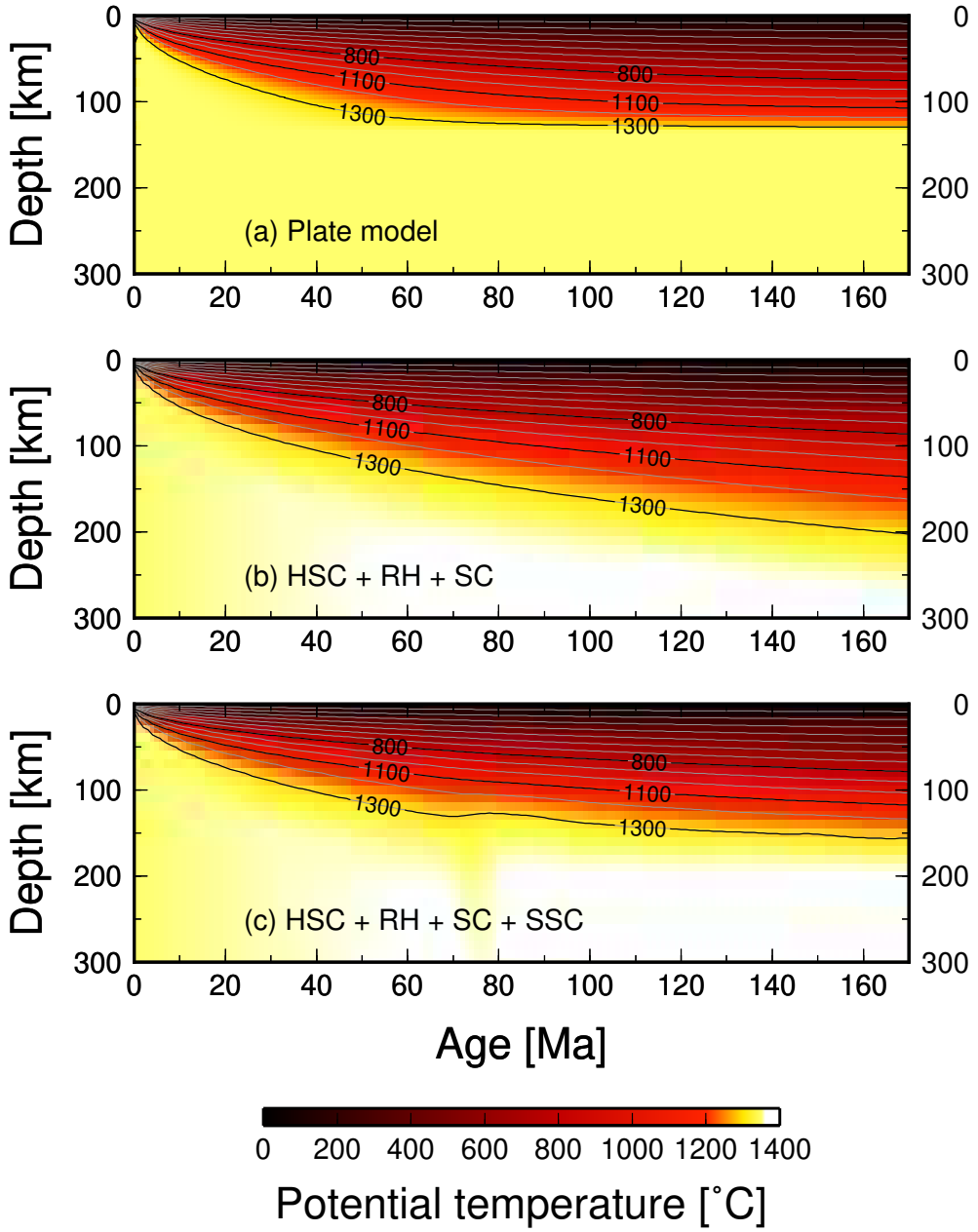

Figure 11. (a) Thermal evolution of oceanic upper mantle based on the plate model with the plate thickness of 135 km. (b) Same as (a), but based on half-space cooling with an internal heating of 2.3×10^{-12} W kg^{-1} and a secular cooling of 100 K Ga^{-1} (equation 7). This is very similar to the new reference model shown in Figure 9; the only difference is that the effect of variable material properties is not taken into account here. (c) Same as (b), but with additional effect of small-scale convection (ridge-parallel variations are averaged); i.e., the effect of internal heating and secular cooling is also incorporated. Sublithospheric convection initiates around the age of 60 Ma. In all models, the effect of adiabatic compression is not considered, and the initial mantle temperature is set to 1350 °C. Gray contours are drawn at every 100 K, and isotherms of 800 °C, 1100 °C, and 1300 °C are shown in solid.

Supporting Information for "A new reference model for the evolution of oceanic lithosphere in a cooling Earth"

Tomoko Korenaga[1], Jun Korenaga[1], Hitoshi Kawakatsu[2], and Makoto Yamano[2]

[1]Department of Earth and Planetary Sciences, Yale University, New Haven, Connecticut, USA

[2]Earthquake Research Institute, University of Tokyo, Tokyo, Japan

Contents of this file

Text S1.

The numerical modeling of mantle convection that is shown in Figure 2 as well as Figures S1-S3 is conducted by solving the following nondimensionalized governing equations for thermal convection of an incompressible fluid, which consist of the conservation of mass,

$$\nabla \cdot \mathbf{u}^* = 0, \tag{1}$$

the conservation of momentum,

$$-\nabla P^* + \nabla \cdot [\eta^* (\nabla \mathbf{u}^* + \nabla \mathbf{u}^{*T})] + RaT^* \mathbf{e}_z = 0, \tag{2}$$

and the conservation of energy,

$$\frac{\partial T^*}{\partial t^*} + \mathbf{u}^* \cdot \nabla T^* = \nabla^2 T^* + H^*. \tag{3}$$

Here asterisks denote nondimensional variables. The spatial coordinates are normalized by the system depth D, and time is normalized by the diffusion time scale, D^2/κ, where κ is thermal diffusivity. Velocity $\mathbf{u}^*$ is thus normalized by κ/D. Dynamic pressure P^* and viscosity η^* are normalized by $\eta_0 \kappa/D^2$ and η_0, respectively, where η_0 is a reference viscosity at $T^* = 1$. Temperature T^* is normalized by a temperature contrast ΔT between the top and bottom boundaries. The unit vector pointing upward is denoted by $\mathbf{e}_z$. The Rayleigh number Ra is defined as

$$Ra = \frac{\alpha \rho_0 g \Delta T D^3}{\kappa \eta_0}, \tag{4}$$

where α is thermal expansivity, ρ_0 is reference density, and g is gravitational acceleration. The Rayleigh number is a nondimensional parameter. Heat generation H^* is defined as

$$H^* = \frac{\rho_0 H D^2}{k \Delta T} \tag{5}$$

where H is heat production rate per unit mass, and k is thermal conductivity.

The governing equations are solved by the 2-D finite element code of (Korenaga & Jordan, 2003). A constant velocity is imposed on the top boundary, whereas the bottom boundary is free slip. The top and bottom temperatures are fixed to 0 and 1, respectively. A reflecting boundary condition (i.e., free slip and insulating) is applied to the side boundaries. The aspect ratio of a model is four. The model is discretized by 256$\times$64 quadrilateral elements, and the elements are refined near the top and the right boundaries to treat the evolution of the thermal boundary layer accurately. For mantle rheology, the following linear exponential form is used:

$$\eta_T^* = \exp[\theta(1 - T^*)], \tag{6}$$

where the Frank-Kamenetskii parameter, θ, controls the degree of temperature dependence, and it is related to the activation energy E as

$$\theta = \frac{E\Delta T}{R(T_s + \Delta T)^2}, \tag{7}$$

where R is the universal gas constant and T_s is the surface temperature. In addition to this temperature-dependent viscosity, a weak zone is introduced at the top-right corner of the model domain, where the nondimensional viscosity is set to unity. This weak zone is necessary to simulate subduction with prescribed plate motion and purely temperature-dependent viscosity (e.g., Huang & Zhong, 2005).

The initial temperature field is set uniformly to 1, and we use a time-invariant internal heat production. When surface heat flux is higher than internal heat production, the system is out of thermal equilibrium and exhibits secular cooling. When a convection model is run with a prescribed plate motion, plate velocity has to be chosen carefully (for a given Ra) to obtain a reasonable thermal structure for a subduction zone. For Ra = 10^9, a nondimensional velocity

of ∼5000 seems appropriate. We dimensionalize model results using D of 2.9×10^6 m, κ of 10^{-6} m^2 s^{-1}, ΔT of 1450 K, g of 9.8 m $^{-2}$, α of 2×10^{-5} K^{-1}, ρ_0 of 4400 kg m^{-3}, and k of 4 W K^{-1} m^{-1}. With this dimensionalization, the Rayleigh number of 10^9 is equivalent to η_0 of $\sim 3 \times 10^{19}$ Pa s, and a nondimensional velocity of 5000 corresponds to 5.43 cm yr^{-1}. We use a nondimensional heat production of 10, which translates to 1.57×10^{-12} W kg$^{-}-1$. With this mount of internal heating, the system exhibits secular cooling at a rate of ∼40-50 K Ga^{-1} (Figure S1a and S1b). The subsidence curves shown in Figure 2g and 2h are scaled so that the pure half-space cooling case has a subsidence rate of 320 m Ma$^{-1/2}$.

The internal heating ratio, which is defined as the difference between top and bottom heat flows normalized by the top heat flow, is ∼0.6, which is lower than the Earth-like value (∼0.87) (Korenaga, 2008), and this is probably because the role of the bottom heat flow is overemphasized in modeling with the Cartesian coordinates than that with the spherical coordinates. Figure 2a and 2b show the snapshots at 3.66 Ga and 1.85 Ga, respectively; these times are chosen so that both snapshots have similar internal temperatures (Figures S1a and S1b) to facilitate comparison. Absolute times themselves do not mean much, because the evolution of transient solutions depends on initial conditions. For comparison, Figures S2 and S3 show snapshots a few hundred million years before and after those shown in Figure 2.

Whereas it may be more desirable to model subduction in a dynamically more self-consistent manner, i.e., without prescribing surface velocity, it is difficult to control the location of subduction in such modeling; the locations of ridge and trench become nonstationary, with time-varying plate sizes. Ideally, both plate velocity and internal heat generation should be allowed to vary with time, but it would further increase the number of model parameters to be adjusted,

and we deem that these examples are sufficient to illustrate likely complications associated with mantle convection with internal heating and secular cooling.

References

Huang, J., & Zhong, S. (2005). Sublithospheric small-scale convection and its implications for residual topography at old ocean basins and the plate model. *J. Geophys. Res.*, *110*, B05404, 10.1029/2004JB003153.

Korenaga, J. (2008). Urey ratio and the structure and evolution of Earth's mantle. *Rev. Geophys.*, *46*, RG2007, doi:10.1029/2007RG000241.

Korenaga, J., & Jordan, T. H. (2003). Physics of multiscale convection in Earth's mantle: Onset of sublithospheric convection. *J. Geophys. Res.*, *108*(B7), 2333, doi:10.1029/2002JB001760.

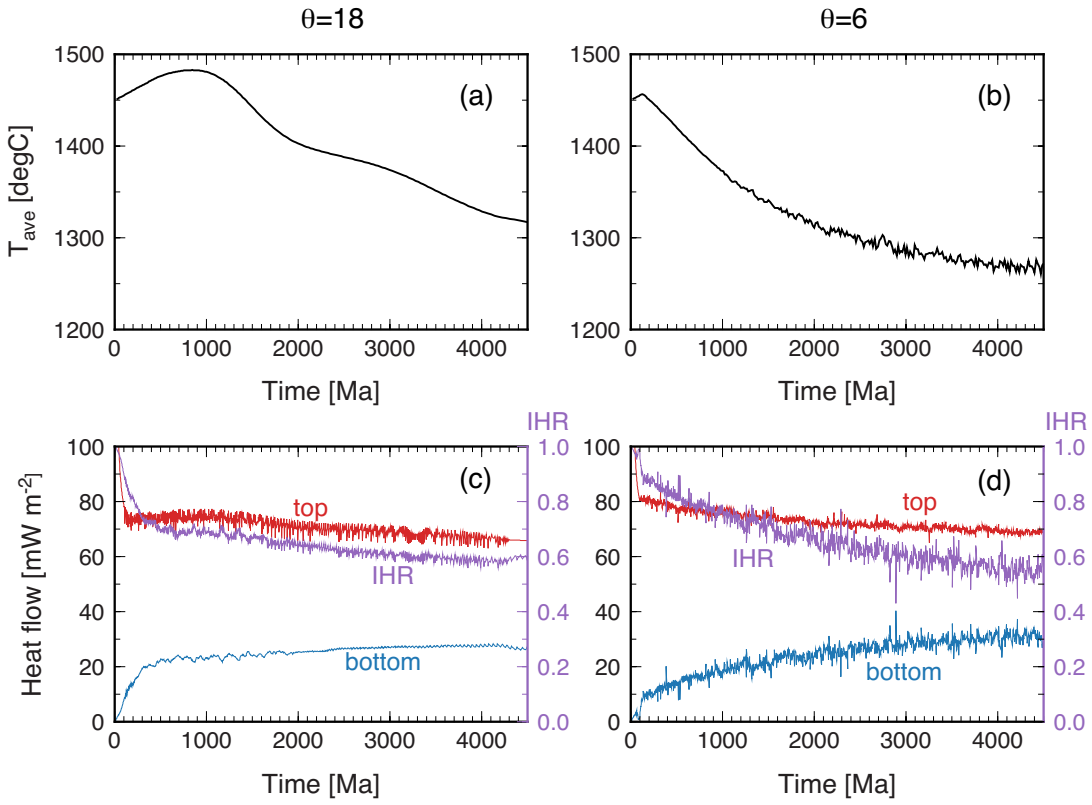

Figure S1. (a) Secular cooling represented by the temperature of the mantle beneath the ridge axis averaged over the depths of 700 km and 2100 km for the case of θ=18. (b) Same as (a) but for the case of θ=6. (c) Heat flow through the top (red) and bottom (blue) boundaries as well as the internal heating rate (purple). (d) Same as (c) but for the case of θ=6.

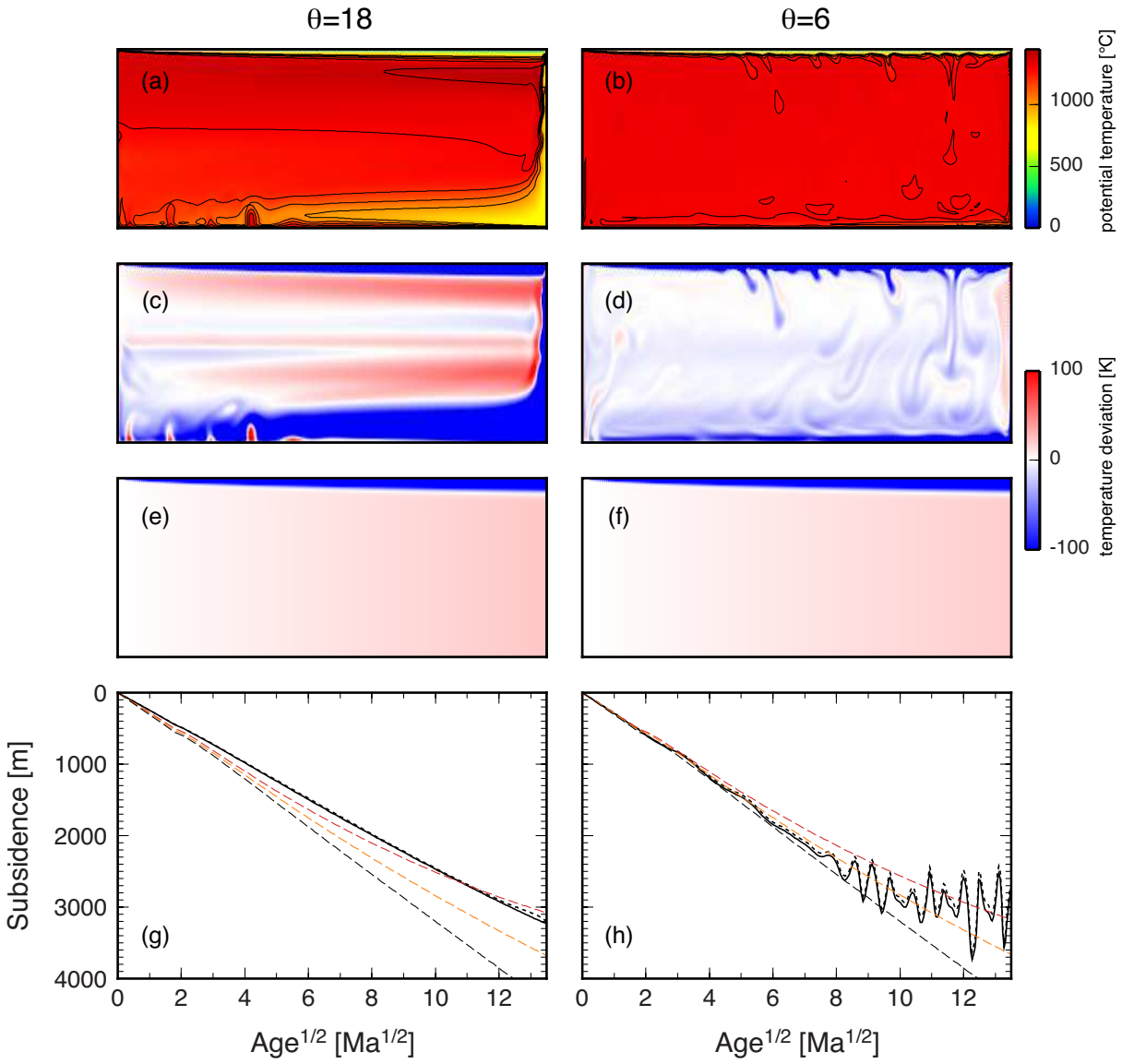

Figure S2. Same as Figure 2, but for snapshots at 3.38 Ga (θ=18) and at 1.69 Ga (θ=6).

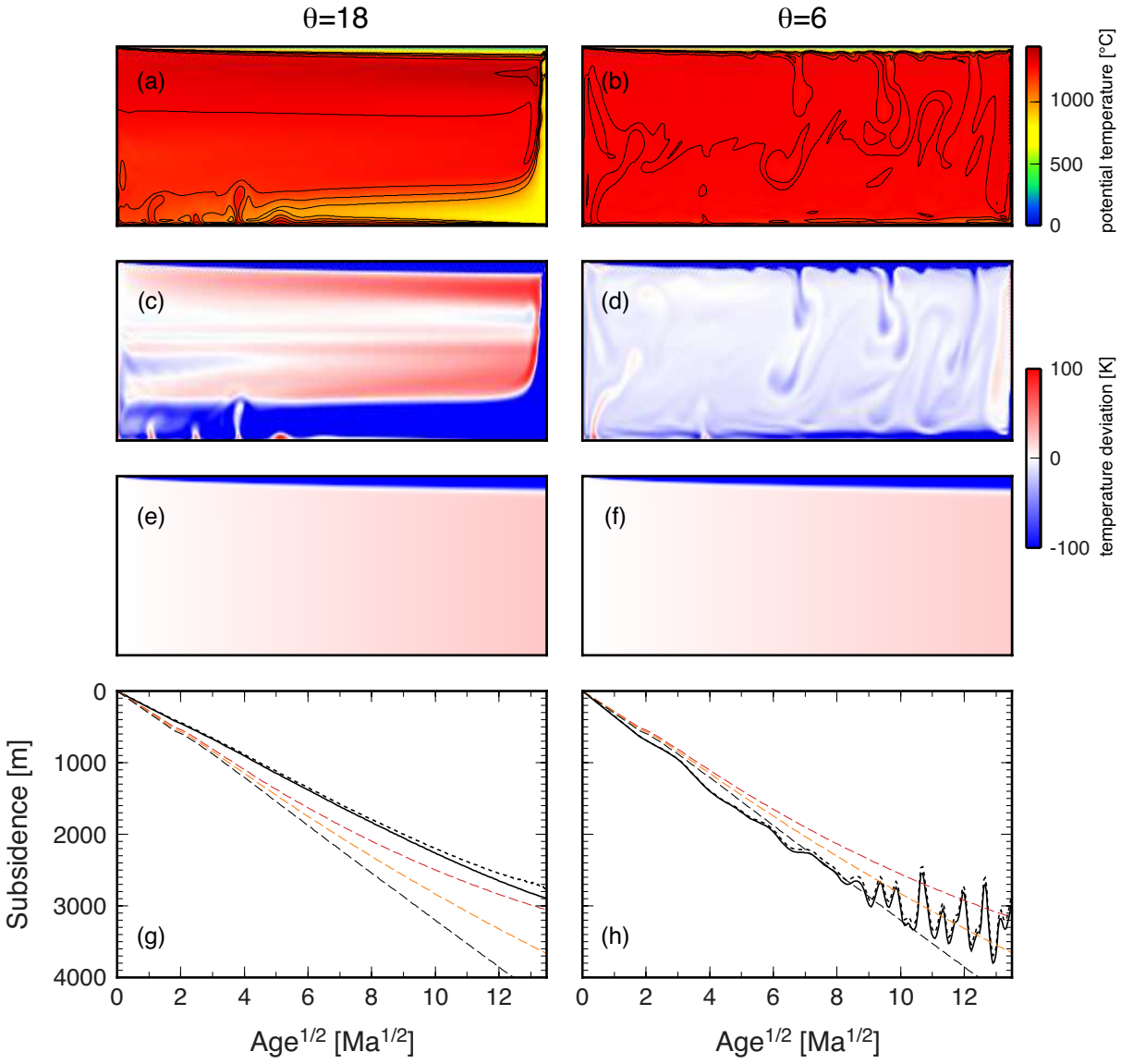

Figure S3. Same as Figure 2, but for snapshots at 3.95 Ga (θ=18) and at 2.02 Ga (θ=6).

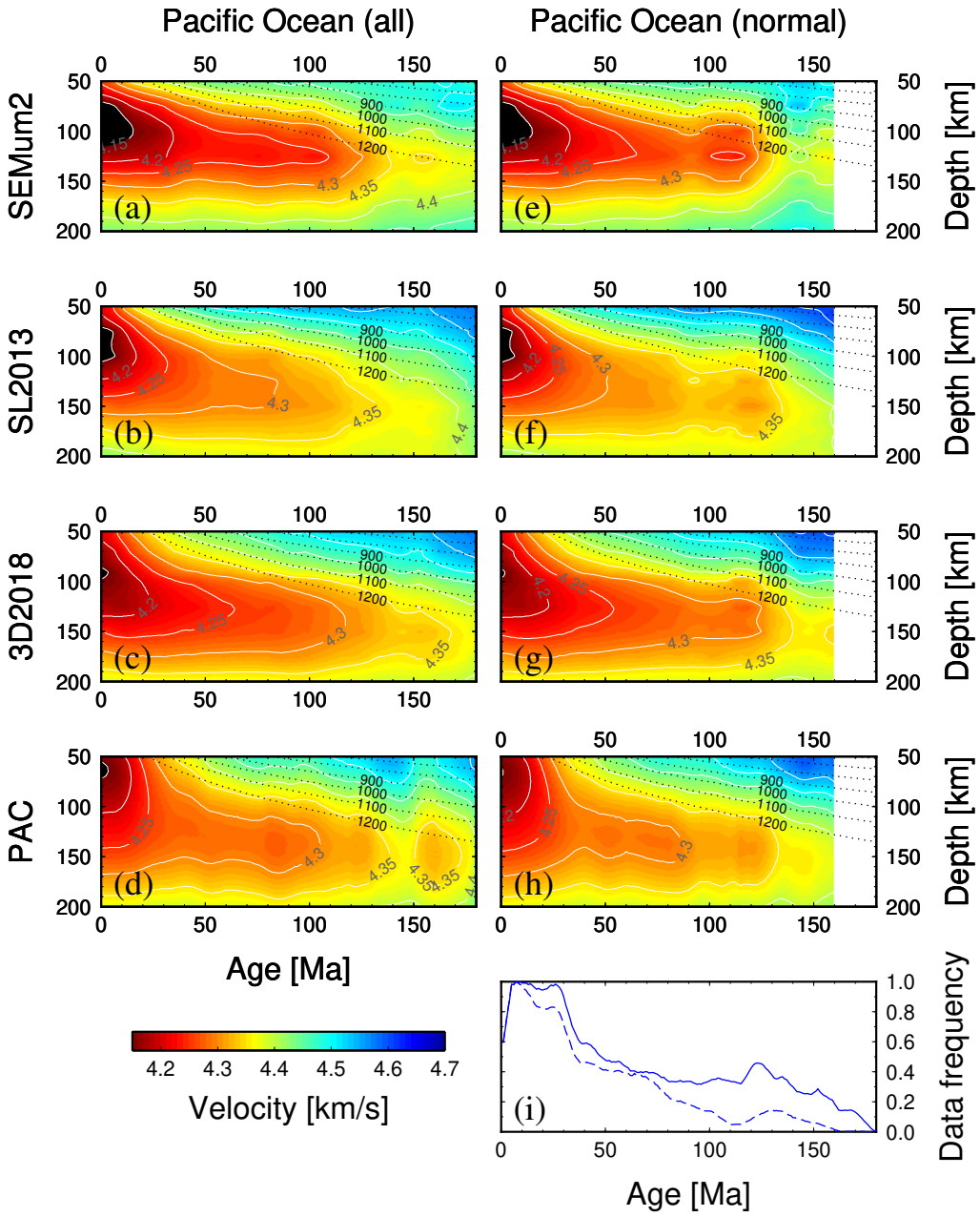

Figure S4. Age-stacked V_{SV} models calculated from four different surface tomography models: (a,e) SEMum2 (French et al., 2013), (b,f) SL2013 (Schaeffer & Lebedev, 2013), (c,g) 3D2018 (Debayle et al., 2016), and (d,h) PAC-age (Isse et al., 2019). This is the same as Figure 8, except that only the Pacific upper mantle is considered for all models.